



RESEARCH ARTICLE

10.1029/2024JD042312

Atmosphere Response to an Oceanic Submesoscale SST Front: A Coherent Structure Analysis

Hugo Jacquet¹ , Alex Ayet² , and Fleur Couvreur³ 

¹CNRS, IGE, Université Grenoble Alpes, Grenoble, France, ²CNRS, Inria, Grenoble INP, GIPSA-Lab, Université Grenoble Alpes, Grenoble, France, ³Météo-France, CNRS, CNRM, Université de Toulouse, Toulouse, France

Key Points:

- Idealized large eddy simulation of the atmosphere over an oceanic submesoscale sea surface temperature front is produced
- Surface winds increase on warm water by the downward momentum mixing mechanism
- An enhanced compensating subsidence is highlighted by a coherent structure analysis based on passive tracers

Supporting Information:

Supporting Information may be found in the online version of this article.

Correspondence to:

H. Jacquet,
hugo.jacquet.work@gmail.com

Citation:

Jacquet, H., Ayet, A., & Couvreur, F. (2025). Atmosphere response to an oceanic submesoscale SST front: A coherent structure analysis. *Journal of Geophysical Research: Atmospheres*, 130, e2024JD042312. <https://doi.org/10.1029/2024JD042312>

Received 30 AUG 2024

Accepted 22 JAN 2025

Abstract The atmosphere response to oceanic submesoscale sea surface temperature (SST) fronts is neither resolved by operational nor climate models. Above the ocean, the atmospheric boundary layer (ABL) is in a convective regime and its turbulence levels and structure are altered by the SST variations. Using large eddy simulations, we investigate an ABL flowing above a 1D oceanic submesoscale SST front. The organization of atmospheric turbulence evolves from rolls to a cell-roll transition state but with a 3.5 km delay due to the strong advection. The SST gradient imprints on the atmosphere, creating a pressure gradient that accelerates the flow at all altitudes. On warm water, horizontal wind in the lower half of the ABL increases mainly due to turbulent mixing. Most of the flow is resolved, and we relate statistical quantities to coherent structures using a conditional sampling. The SST increase strengthens updrafts, whereas a downward motion develops in response, transporting high wind from the upper to the lower layers of the ABL. We show that this descending flow is not a downdraft but rather a less turbulent object similar to an enhanced compensating subsidence, which could be parametrized by a mass-flux term. The intense updrafts overshoot the boundary layer height and could trigger convection with moister environmental conditions.

Plain Language Summary Ocean and atmosphere exchange heat, moisture, and momentum at their interface on a very wide range of scales. In this study, we focus on understanding the processes that take place in the atmospheric boundary layer above submesoscale (less than 10 km) and abrupt changes in sea surface temperature. These small scales are parameterized in climate and forecast models. We use a numerical simulation that resolves most of the flow and detect coherent structures in this flow. Coherent structures are objects that consist of an aggregate of air parcels that carry the bulk of vertical flux. Using this tool, we show that thermals are greatly enhanced on warmer water but with a lag due to the strong wind in this configuration. They induce an increase in wind near the surface, consistently with observations from satellite data or with other simulations.

1. Introduction

The complex coupling between the ocean and the atmosphere is scale dependent. At the ocean basin scale, the atmosphere drives ocean mixing and currents. At oceanic mesoscale (10–100 km), ocean eddies or boundary currents structure the sea surface temperature (SST). This affects the atmospheric boundary layer (ABL) stability and hence ABL properties. Satellite observations (Krug et al., 2018; O'Neill et al., 2012) show that surface stress and wind increase above warm water and decrease over cold water. This behavior has been reproduced in atmospheric models (Kilpatrick et al., 2014, 2016; Lambaerts et al., 2013) and in a coupled model (Perlin et al., 2020).

Two mechanisms have been suggested to explain this increase in surface wind speed: (a) the downward momentum mixing (DMM) mechanism (Wallace et al., 1989), an enhancement of turbulent mixing in the ABL over warm water leading to an increase in lower-layer winds and a decrease in higher-layer winds; (b) the pressure adjustment (PA) mechanism (Lindzen & Nigam, 1987), which is similar to a sea breeze. The SST imprints its temperature gradient into the ABL, forming a horizontal pressure gradient that induces a secondary circulation toward the warmer side of the SST front. The relative importance of those two mechanisms depends on environmental conditions: high (slow) wind speed, weakly (strongly) unstable environment or a sharp (smooth) front will favor the DMM (PA) mechanism (Ayet & Redelsperger, 2019; Foussard et al., 2019; Lambaerts et al., 2013). To go beyond these environmental parameters, Ayet and Redelsperger (2019) derived an analytical model that takes into account both the DMM and PA mechanisms. They show that the shape of turbulent stress inside the

© 2025 The Author(s).

This is an open access article under the terms of the [Creative Commons Attribution-NonCommercial License](https://creativecommons.org/licenses/by-nc/4.0/), which permits use, distribution and reproduction in any medium, provided the original work is properly cited and is not used for commercial purposes.

ABL is essential in setting the relative importance of PA or DMM mechanisms. This highlights the need for turbulence-resolving simulations of the ABL to accurately describe ABL-SST interactions.

The atmosphere response to oceanic submesoscale (<10 km) SST fronts has been much less investigated. It is dependent on scales that are parametrized in cloud resolving models (Lambaerts et al., 2013) and requires large eddy simulations (LES) to capture the fine scales at play (Ayet et al., 2021; Redelsperger et al., 2019; Skillingstad et al., 2007; Sullivan et al., 2020, 2021; Wenegrat & Arthur, 2018). Skillingstad et al. (2007) and Sullivan et al. (2020) (S20 hereafter, note that this study will serve as a reference in the following) focused on idealized across-front configurations in a dry atmosphere with both cold to warm and warm to cold transitions. In contrast, Redelsperger et al. (2019) used a realistic configuration in the Iroise Sea with an hourly simulated SST forcing. They found that the DMM was the primary source of increased surface wind speed over warm water, whereas the pressure gradient term was less important (~20% of the vertical mixing term in Skillingstad et al. (2007)). S20 showed a nonlinear response of the atmosphere with a “thermal overshoot” of the sensible heat flux, shifted by advection. The increase in sensible heat flux leads to turbulence reaching levels higher than the mean ABL height. This induces stronger entrainment of air from above the boundary-layer height into the boundary layer and could influence cloud formation (Desbiolles et al., 2021).

These LES studies have focused primarily on analyzing the averaged momentum budget. The PA and DMM mechanisms are diagnosed through the presence of secondary circulations and the relative importance of the pressure and turbulent mixing terms in this budget. Two shortcomings might be identified in these studies. First, the consequences of the PA and DMM mechanisms have not been investigated. At the ocean mesoscale, the PA and DMM mechanisms imply a linear link between wind divergence and the SST gradient (for DMM) or SST Laplacian (for PA). This linear link might break at submesoscales where other terms appear in the mean momentum balance (Ayet & Redelsperger, 2019; Villas Bôas et al., 2019). Second, less is known on the effects of these small-scale SST changes on turbulence itself. However, changes in the instantaneous structure of turbulence are observed (e.g., Figure 5 of S20, and Ayet et al. (2021)). Those have not been linked to their average effect in the mean momentum budget (e.g., the PA and DMM mechanisms). This is foremost a fundamental question, since we expect submesoscale SST variations to strongly act on turbulence scales and change its structure (as opposed to coarser heterogeneities, Nuijens et al. (2024)). It is also of practical importance, since understanding the link between instantaneous turbulent structures and their averaged effect is essential to interpret high resolution satellite (Ayet et al., 2021) and plane measurements (Brilouet et al., 2023) in which the effect of the submesoscales on turbulence is measurable.

Linking the instantaneous and mean flow can be achieved by a conditional sampling of the flow. The choice of the sampling operator offers varying degrees of interpretability: (a) Schmidt and Schumann (1989) and Dixit et al. (2021) used the vertical velocity to detect upward or downward momentum-transporting structures. This method depends on an ad-hoc reference value for the vertical velocity, and it also detects internal gravity waves in the entrainment zone; (b) Lin et al. (1996) and Sullivan et al. (1998) used a quadrant analysis, which computes the joint probability distributions of several fluctuations. It can help identify turbulent structures that contribute significantly to turbulent fluxes. This decomposition is not unique and depends on the fluctuations chosen: quadrants identified with the fluctuations u' and w' are different from the quadrants detected with w' and θ' . Sometimes a minimum amplitude of the flux is defined, and this threshold is arbitrary; (c) Adrian (1996) proposed a method to estimate conditionally averaged quantities of a flow by using a linear stochastic estimate. This method is based on the correlation of a flow variable with an event, usually an instantaneous structure, and is cheap numerically.

Conditional objects are weakly dependent on the event type and location. The main disadvantage of the method is that if the flow presents a wide distribution of properties (shape, spacing between features, and angle of inclination) for the same event then the estimated conditionally averaged object would be less representative of the actual instantaneous event used to compute the correlation function (Christensen & Adrian, 2001). In the context of ABL flows, Couvreur et al. (2010); Brient et al. (2024); Weinkaemmerer et al. (2023) used a passive tracer to identify label coherent objects and explore their contribution to conditionally averaged quantities. This method is interesting because it gives a decomposition of the instantaneous flow, which can be used to investigate processes in specific layer of the ABL (e.g., the entrainment zone). It also relies on a less arbitrary threshold than method (a) although some parameters still need to be defined by the user. This method requires the emission of passive

tracers, which is only possible in a numerical simulation and not in observations and adds to the total cost of the simulation the steps to iterate the tracer equation evolution.

In the following, we investigate the instantaneous atmospheric turbulent response to a submesoscale across-front configuration using idealized LES simulations and the sampling method developed by Couvreur et al. (2010). We aim to answer the following questions:

1. Are the DMM and PA mechanisms and their consequences also present at the oceanic submesoscale? Are there other processes that should be considered?
2. Can instantaneous coherent structures explain momentum and scalars mixing in the ABL interior? How are these objects related to the DMM and PA mechanisms?

This manuscript is organized as follow: the model and numerical setup of the simulations are described in Section 2. In Section 3, we present the mean equations of the flow and the conditional sampling used for the coherent structure analysis. In Section 4, results are presented with an analysis of the turbulent structures and their contribution to the vertical fluxes. Finally, results are discussed, and this manuscript is concluded by a conceptual view that summarizes the most important physical processes evidenced with this numerical experiment.

2. Simulation Setup

2.1. The Atmospheric Model

In this study, we use the atmospheric model Meso-NH (Lac et al., 2018; Lafore et al., 1998) version 5.6.2, a multi scale non-hydrostatic model, here in LES configuration, with the pseudo-incompressible formulation of the continuity equation from Durran (1989). The wind variables (u, v, w) are advected with a fourth order centered scheme, whereas the meteorological variables (mixing ratios, temperature and subgrid Turbulent Kinetic Energy (subgrid TKE)) are advected with a piece-wise parabolic method. The temporal integration is done by a fourth order Runge-Kutta integration. An effective resolution of $4\Delta x$ is expected with this choice of schemes. In LES, most of the eddies are explicitly resolved by the model while subfilter (or more usually subgrid) turbulent fluxes have to be parametrized. The closure used in the model is the 1.5 order closure proposed by Cuxart et al. (2000): the subgrid TKE is a prognostic variable and a length scale is computed as a diagnostic. Both are used to compute the second order subgrid fluxes with a stability dependent term. In this study, the length scale is set as the mixing length proposed by Deardorff (1980) where the atmosphere is strongly stratified and the cubic root of the cell volume elsewhere. The surface boundary conditions are given by the SURFEX platform (Masson et al., 2013) and computed by the COARE3 iterative algorithm (Fairall et al., 2003) and the SST is prescribed. Radiative processes have not been taken into account in this study. Clouds can form, following the microphysic parametrization of ICE3 (Caniaux et al., 1994; Pinty & Jabouille, 1998). Following Couvreur et al. (2010), passive tracers are emitted at the surface and on top of the boundary layer to characterize coherent structures of the flow. They follow a radioactive decay to avoid accumulation of tracer.

2.2. Geometry and Initial Conditions

The simulation setup is similar to S20: we simulate an across front wind over an SST front with similar gradient. Unlike S20, moisture is included in our setup and contributes to buoyancy. We aim to observe a transition of the ABL from weakly unstable to even more unstable ABL. An important difference between S20 and our simulation is the boundary conditions at the west (inflow) and east (outflow) boundaries: they are periodic, as opposed to open in S20. Open boundary conditions are the first choice when designing a fluid simulation over a heterogeneity, as they allow for an inflow that is not influenced by the heterogeneity. The simplest open boundary condition only inputs profiles into the simulation without introducing any turbulent variability. This is prohibitively expensive as it requires a very long domain in the mean wind direction to ensure developed turbulence before the change of SST. The “Fourier Fringe” method used in S20 allows for a turbulent inflow with open boundary conditions: turbulent intensity (i.e., flux profiles) can be prescribed. Since this method is not yet implemented in MesoNH version 5.6.2, we use periodic boundary conditions much like the setup from Fogarty et al. (2024) above a sea-ice heterogeneity. This implies that the flow keeps some memory of its previous crossing of the SST front (this will be discussed in Section 4.1).

In the following, S20 will be used as a reference. Despite the boundary conditions, essential elements of the atmospheric response to a cold to warm SST front described in S20 appear in our simulation: the evolution from a

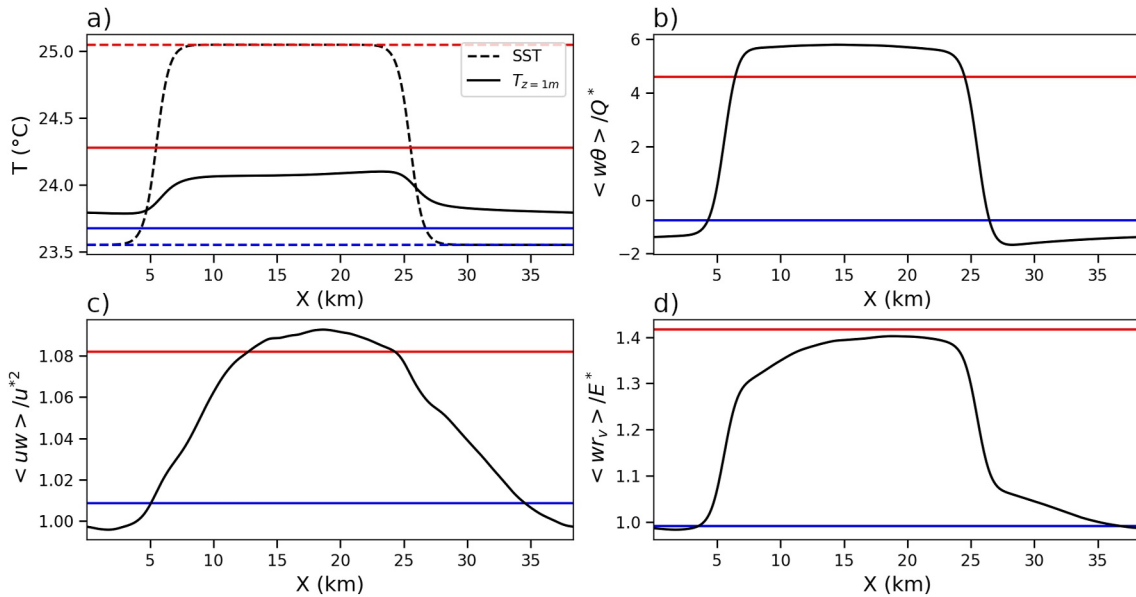


Figure 1. Surface quantities in the S1 simulation (black) and the reference simulations (red for RefW, blue for RefC). (a) Sea surface temperature (dashed line) and atmospheric temperature at first level (solid line); (b) Normalized sensible heat flux; (c) Normalized friction velocity; (d) Normalized latent heat flux. All fluxes are computed at first model level and have been normalized by their absolute value from S1 at $X = 4$ km (just before the SST jump).

roll to a cell-roll transition state (Section 4.1), the evolution along X of the zonal wind budget (Section 4.2) and the increase of entrainment at the “thermal overshoot” (Section 4.4.3).

The simulation S1 dimensions are 38.4, 8, 2 km in the X (along flow), Y (across flow), and Z (vertical) directions, respectively. The horizontal resolution is 50 m ($\Delta x = \Delta y$) and the vertical resolution ranges from $\Delta z = 2$ m to $\Delta z = 20$ m with 15 cells under the altitude of 60 m. Resolved turbulence is 80% or more of the total turbulence from 60 m and above.

The top of the model uses a free slip condition together with a sponge layer to suppress gravity waves. Lateral boundary conditions are cyclic and the surface condition is a no slip condition (model first level winds are given by the SURFEX platform). The SST is prescribed and kept constant for the entire simulation. The SST is homogeneous in the Y direction and varies along X with a profile of the form (see Figure 1a, dark dashed line):

$$\text{SST}(x) = T_0 + \Delta T/2 \cdot \left[\tanh\left(\frac{x - (x_1 + L_1/2)}{L_1}\right) - \tanh\left(\frac{x - (x_2 + L_2/2)}{L_2}\right) \right] \quad (1)$$

with $T_0 = 296.55$ K the temperature of the coldest SST, $\Delta T = 1.5$ K the jump of temperature from cold to warmest SST, x_i and L_i the position and width of the i th front, x_i is chosen as the position where $\text{SST} = T_0 + \Delta T/2$. $x_1 = 5$ km, $x_2 = 25$ km and $L_1 = L_2 = 1$ km. The SST front is shown in Figure 1a and consists of two transition zones: a cold to warm front and a warm to cold front. The “cold SST” zone will be referred as X positions where $X \in [0, 4]$ km \cup $[26, 38.4]$ km and the “warm SST” zone refers to X positions where $X \in [6, 24]$ km. The SST gradient is ~ 1.5 K.km $^{-1}$ in this configuration and is of similar intensity as most of the fronts (2 K over less than a few kilometers) observed by Singh Khalsa and Greenhut (1989) near Bermuda, although they also observed stronger fronts (2 K over 100 m).

Alongside this numerical experiment, two other reference simulations have been run: RefC with uniform SST corresponding to the zone with cold SST (296.55 K) and RefW with uniform SST from the warm SST (298.05 K) (Figure 1a).

All simulations are initialized with the following atmospheric conditions: an initial mixed boundary layer (height $z_i = 250$ m) with constant potential temperature ($\theta_c = 295.5$ K) and vapor mixing ratio ($r_{v,c} = 10$ g.kg $^{-1}$) under z_i and a linearly increasing (decreasing) potential temperature (mixing ratio) of 3 K.km $^{-1}$ ($-4, 6$ g.kg $^{-1}$.km $^{-1}$). Note

Table 1
Turbulent Characteristics for the Simulation S1, RefW and RefC, and the Simulations From S20

Name	Ug	Q_v^*	Q^*	E^*	u^*	w^*	z_i	$-z_i/L$
S1 (cold)	(7.5, 0)	0.00653	-0.00147	0.04445	0.212	0.504	600	5.38
S1 (warm)	(7.5, 0)	0.01939	0.00817	0.06183	0.230	0.724	600	12.51
Ref W	(7.5, 0)	0.01819	0.00676	0.06296	0.229	0.750	709	14.05
RefC	(7.5, 0)	0.00683	-0.0011	0.04403	0.213	0.491	531	4.59
S20 (entry)	(10, 0)	-	0.0120	-	0.284	0.602	560	3.74
Es2 (end)	(10, 0)	-	-0.0016	-	0.234	0.310	560	-0.96
Eu2 (end)	(10, 0)	-	0.0360	-	0.301	0.870	560	9.91

that the value of T_0 is set equal to the initial air temperature at the first model level, as the value of T_0 sets the regime of turbulence of the atmosphere. We aim to get a convective regime for the ABL even on the coldest part of the SST. Ultimately, the surface temperature warms up (Figure 1a, full black line) and this results in a thin layer of the atmosphere where the cold SST region thermally stabilizes the air. A constant wind field $(U, V, W) = (7.5, 0, 0)$ m.s⁻¹ is used both as initial condition and as geostrophic wind. The Coriolis parameter is set to $f = -8.47e-5$ s⁻¹. The values of the geostrophic wind and the Coriolis parameter are inspired by the numerical setup from Ayet et al. (2021) who simulated a realistic midlatitude submesoscale SST front. Initial thermodynamic conditions are adapted from the ERA5 reanalysis profiles in the same zone.

Table 1 summarizes the turbulent characteristics for the S1 simulation at $X = 4$ km (cold) and $X = 23$ km (warm) as well as for the Ref W and RefC. It also includes data from the two one-front configurations of S20, called Eu2 and Es2. S1 and Eu2 will be compared in detail in Section 4.1. Inflow statistics for the simulations from S20 are denoted as S20 (entry), and they are common for their simulations Eu2 and Es2. Table 1 entries for Eu2 (end) and Es2 (end) are taken at 20 km downwind of the inflow for the Eu2 and Es2 simulations, respectively. U_g is the geostrophic wind (m.s⁻¹), Q_v^* is the buoyancy flux (K.m.s⁻¹), Q^* is the sensible heat flux (K.m.s⁻¹), E^* is the latent heat flux (g.kg⁻¹.m.s⁻¹), u^* is the friction velocity (m.s⁻¹), w^* is the convective velocity (m.s⁻¹), z_i is the boundary layer height (m). $L = \frac{\theta_{s0} u^{*3}}{\kappa g Q_v^*}$ is the Monin-Obukhov length, $\kappa = 0.4$ is the von Kármán constant and $\theta_{s0} = 300$ K. All fluxes in this table are calculated using the total flux (resolved + subgrid) at first model level. In the following, normalization will be done using values from S1 (cold) (first row in Table 1).

A spin-up is run for 2 hr and statistics are computed with data over 1 hr from the first to the second hour. The 1 hr period used for statistics corresponds to ~ 3 large eddy turnover times $\left(t^* = z_i/w^*, \text{ with } w^* = \left[\frac{g z_i}{\theta_{s0}} Q_v^* \right]^{1/3} \right)$ on the cold water and ~ 5 t^* on warm water. We diagnose the ABL height as the height where the vertical gradient of virtual potential temperature is maximum, this gives an entrainment zone not centered on z_i but slightly lower (Sullivan et al., 1998). In 1 hr, the boundary layer grows and the domain mean ABL height increases linearly from 570 to 640 m. When averaging in time and Y (the average operator is defined in the next section), the top of the boundary layer depends on the X position: the minimum is $z_i = 580$ m (at $X = 10$ km) and the maximum is $z_i = 630$ m (at $X = 28$ km). The ABL height growth is thus 70 m during 1 hr and 60 m along the X dimension and so a unique normalizing height $z_i = 600$ m will be used in this study for all profiles from S1.

3. Methods

3.1. Mean Equations

We define an Reynolds average $\langle . \rangle$ by combining a temporal average from +2 to +3 hr followed by a spatial average in the Y direction (from 0 to 8 km) and finally a running average in the X direction with a small window of 20 cells (1 km). Variables are then partitioned into a mean and turbulent part, $A = \langle A \rangle + a$. Total mean flux are the sum of resolved and subgrid flux: $\langle ab \rangle = \langle \tilde{a}\tilde{b} \rangle + \langle F_{SGS,ab} \rangle$. The equations of continuity, conservation of momentum, and scalar can be written as (Wyngaard, 2010):

Table 2
Labels of the Turbulent Coherent Structures

	$\tilde{s}_1 > 0$	$\tilde{s}_2 > 0$	$\tilde{s}_3 > 0$
$W > 0$	Updraft 1	Updraft 2	–
$W < 0$	Sub. shell 1	Sub. shell 2	Downdraft

$$\frac{\partial \rho_{0eff} \langle U_i \rangle}{\partial x_i} = 0 \quad (2)$$

$$\frac{D \langle U \rangle}{Dt} = -f \cdot \langle V \rangle - \frac{1}{\rho_0} \frac{\partial \langle P \rangle}{\partial x} - \frac{\partial \langle uw \rangle}{\partial z} \quad (3)$$

$$\frac{DC}{Dt} = -\frac{\partial \langle u_i c \rangle}{\partial x_i} \quad (4)$$

where the subscript i in Equations 2 and 4 denotes the three wind components (x, y, z), the subscript 0 denotes the hydrostatic reference state, $\theta_v = \theta \left(1 + \frac{R_v}{R_d} r_v\right) / (1 + r_v)$ with θ the potential temperature, R_d and R_v the gas constant of dry air and water vapor respectively, and r_v the ratio of water vapor density over dry air density. P is the absolute pressure deviation from the reference state. ρ_{0eff} is defined as $\rho_{0eff} = \rho_0 \theta_{v,0} (1 + r_{v,0})$ and is a modified density used in the pseudo-incompressible system of Durran (1989). In Equation 3, the LHS is the total derivative of wind; the RHS terms are from left to right: Coriolis force, pressure gradient force, and turbulent stress divergence. Equation 4 is the conservation of a scalar $C = r_v$ or $C = \theta$ where phase change and radiation are not taken into account. The term on the LHS is the Lagrangian evolution of C , the sum of the local (Eulerian) evolution $\partial C / \partial t$ and the advection of C by the mean wind $\langle U_i \rangle \partial C / \partial x_i$. The term on the RHS is the turbulent scalar divergence.

3.2. Conditional Sampling of the Flow

A conditional sampling method is used to identify turbulent coherent structures following Couvreux et al. (2010) and Brient et al. (2024). Coherent structures are defined here as turbulent objects transporting a passive tracer that tracks the origin of the object. This tool, originally tailored for convective boundary layers (Couvreur et al., 2010), has also been used by Brient et al. (2024) to describe downward-moving structures in a stratocumulus case.

In this study, we adapted the method by emitting three passive tracers (compared to two in Brient et al. (2024)): one on the cold side of the SST (tracer 1), one on the warm side of the SST (tracer 2), and one at the top of the ABL (tracer 3, which is emitted at every instant at the altitude $z_i + 50$ m, across the horizontal domain). All tracers follow a radioactive decay of characteristic time ν to prevent any accumulation. The parameter ν has been set to the convective timescale. A sensitivity study, available in Supporting Information S1, has been conducted to ensure that this choice represents coherent structures in the ABL by maximizing the flux contributions of each structures to the total mean flux.

Conditional sampling (C10 hereafter) is then achieved by first filtering out nonturbulent air cells where tracer fluctuation, with respect to its mean concentration, is smaller than its standard deviation. Then, turbulent structures are labeled based on the sign of the vertical velocity and the sign of tracer fluctuations. The different categories are gathered in Table 2 where \tilde{s} is the resolved tracer concentration fluctuations with respect to its mean value, W is the vertical velocity and “sub. shell” refers to subsiding shells. Both object detection and fluctuations are computed using the resolved flow only. Two parameters appear in the conditional sampling method and are kept identical to those used by Brient et al. (2024) (see their Equations 1–3). Once coherent structures have been labeled, conditionally averaged turbulent statistics (mean, flux) are computed.

The main advantage of the C10 method is that it is based on a less arbitrary threshold to select turbulent areas in the flow (as in e.g., the Q criterion). We use a threshold on the standard deviation of tracer concentration to select only significant fluctuations. What is considered “significant” is still subjective but the standard deviation of tracer concentration does evolve with the studied case. With the second condition (Table 2), the C10 method provides physical meaning to each object by considering two factors: the sign of the vertical velocity and the sign of the tracer concentration fluctuation. Overall, the C10 method provides a way to detect objects that are coherent both spatially (turbulent filter and condition on vertical velocity sign) and temporally (clustering of tracer that goes under radioactive decay).

On top of C10, flux contributions from objects may be again decomposed into a top-hat and an intra-variability parts (Wang & Stevens, 2000). For this decomposition, we consider three disjoint ensembles: “updrafts” (updraft

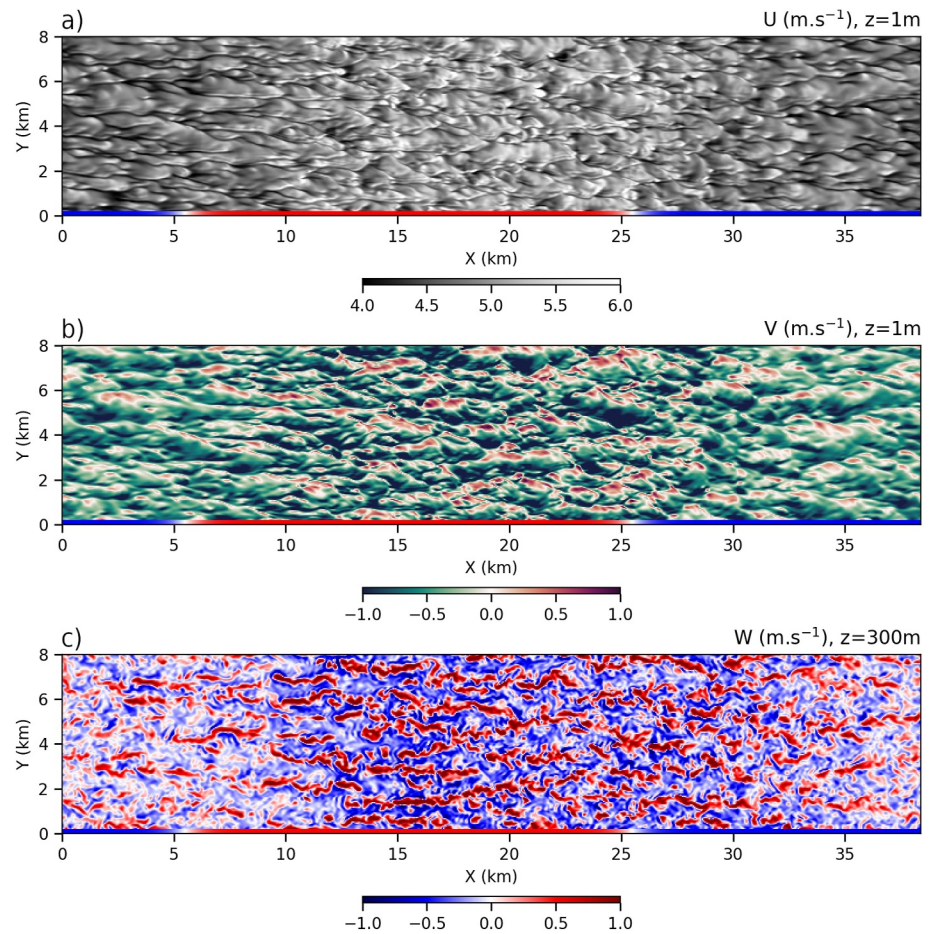


Figure 2. Snapshot at $t = +3$ hr of (a) zonal and (b) meridional wind at first model level and (c) vertical velocity in the middle of the atmospheric boundary layer. The colored line at the bottom of the panels indicates the sea surface temperature with blue representing cold SST (296.55 K) and red warm SST (298.05 K). The cold to warm and warm to cold fronts are located at $X = 5$ km and $X = 25$ km respectively.

1 and updraft 2 have been merged into one for this), “downdrafts”, and “other.” The “other” category includes all coherent structures that are neither “updraft” nor “downdraft” (e.g., subsiding shells), as well as any cells not labeled by C10, ensuring that the sum of all contributions equals the mean flux. The top-hat decomposition then splits each of the object’s contribution to a flux into a nonlocal mixing term (the top-hat part) and a local mixing term (the intra-variability part). Further details about the flux computations and the sensitivity of the radioactive decay on the conditional sampling are provided in Supporting Information S1.

4. Results

4.1. Simulation Overview

In S1, the ABL is always in a convective regime: slightly convective ($-z_i/L = 5.38$) on the cold SST and fairly convective ($-z_i/L = 12.51$) on warm SST. These stability values fall between the values of RefC ($-z_i/L = 4.59$) and RefW ($-z_i/L = 14.05$). In Eu2, the stability parameter before the SST jump (S20 (entry) in Table 1) is $-z_i/L = 3.74$ and it is $-z_i/L = 9.91$ at the end of their domain. Although in S1 the SST jump is only of 1.5 K compared to the 2 K of Eu2, the ABL stability just before the front and far down the front are similar between S1 and Eu2.

Figure 2c shows that the turbulent structures are aligned with the mean wind for $X \in [0, 4]$ km and $X \in [30, 38.4]$ km, corresponding to a flow organized in rolls above the cold SST, whereas for $X \in [4, 30]$ km, the turbulent structures transition from rolls to cells above the warm SST. The Roll Factor diagnostic (Salesky

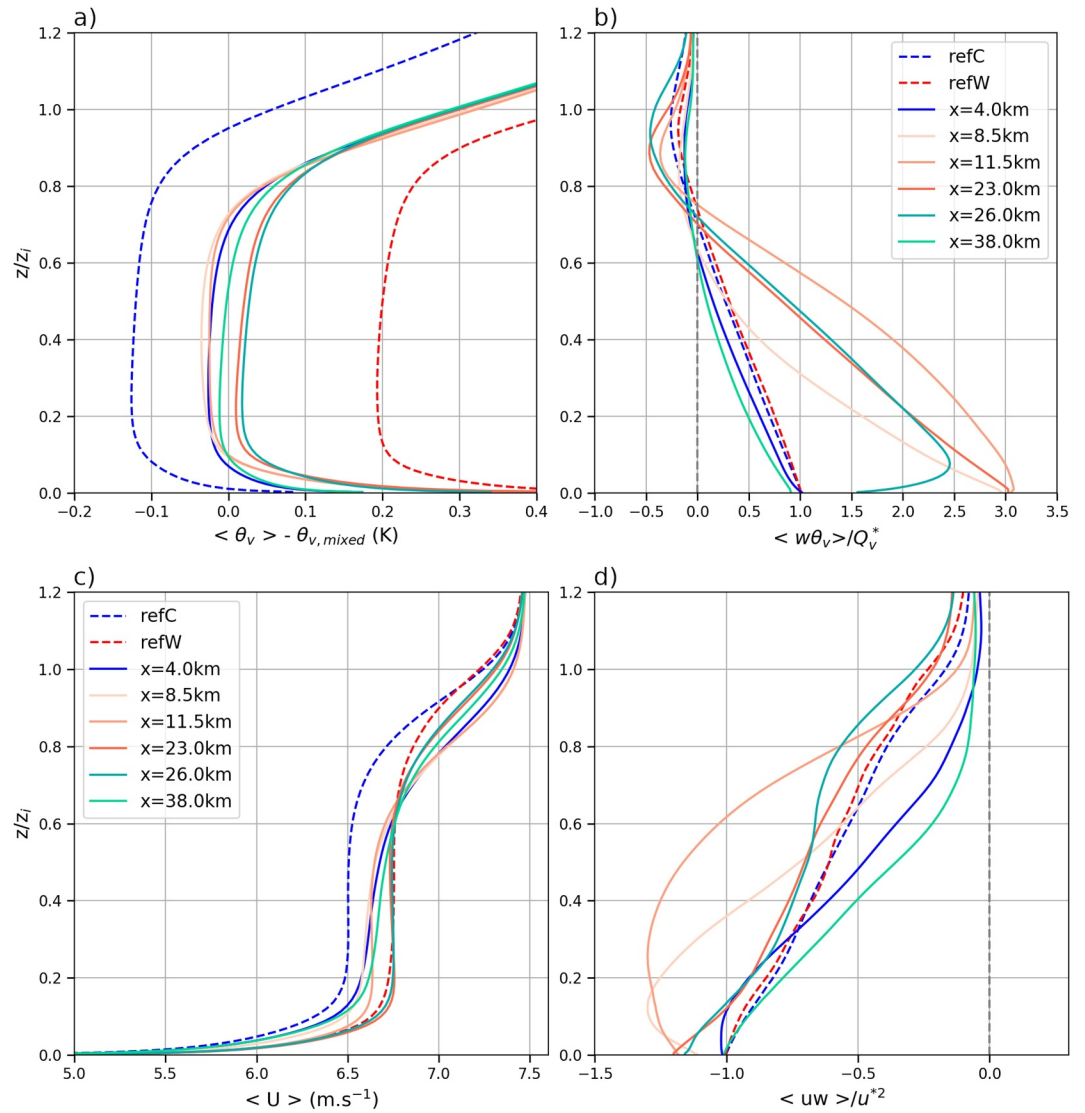


Figure 3. (a) Profiles of virtual potential temperature, (b) total (resolved + subgrid) buoyancy flux, (c) profiles of zonal wind, and (d) total (resolved + subgrid) zonal momentum flux. S1 in full lines and reference simulations in dashed lines. The temperature profiles are plotted as anomaly from the average temperature of the mixed layer of S1 (averaged over the full X domain and between $0.1z_i$ and $0.7z_i$ in vertical, this gives $\theta_{v,mixed} = 297.70$ K). The S1 fluxes are normalized by the surface flux at $X = 4$ km and are plotted at different positions. Reference fluxes are normalized by their horizontally averaged surface values. The altitude is normalized by the domain mean height of the atmospheric boundary layer, $z_i = 600$ m.

et al., 2017), computed on the zonal wind at $Z = 10$ m, is $R = 0.43$ on the cold SST (X from 30 to 38 km) and $R = 0.23$ on the warm SST (X from 15 to 23 km). For comparison, the Roll Factor for the reference homogeneous simulations is $R = 0.49$ for RefC and $R = 0.17$ for RefW. A value of $R > 0.4$ indicates that structures of characteristic size greater than half the boundary layer height exhibit a preferred direction typical of roll organization. In the near-neutral cases (ABL above the cold SST for S1 and refC), the autocorrelation function shows that the preferred direction of surface structures is in the mean wind direction (not shown). These Roll Factor values are consistent with the evolution of the Roll Factor with z_i/L by Salesky et al. (2017).

Virtual potential temperature profiles plotted in Figure 3a are typical of convective boundary layers (Stull, 1988). The mixed layer (ML) extends from $z/z_i = 0.15$ to $z/z_i = 0.75$. Above, S1 shows a weak inversion with a maximum vertical gradient of θ_v of 2.7 K.km^{-1} . The bottom of the entrainment zone is defined as the height where the buoyancy flux profile crosses zero and the top where the flux becomes constant with height. With this definition, Figure 3b shows an entrainment zone depth of roughly $0.35z_i$, which is relatively deep. Additionally,

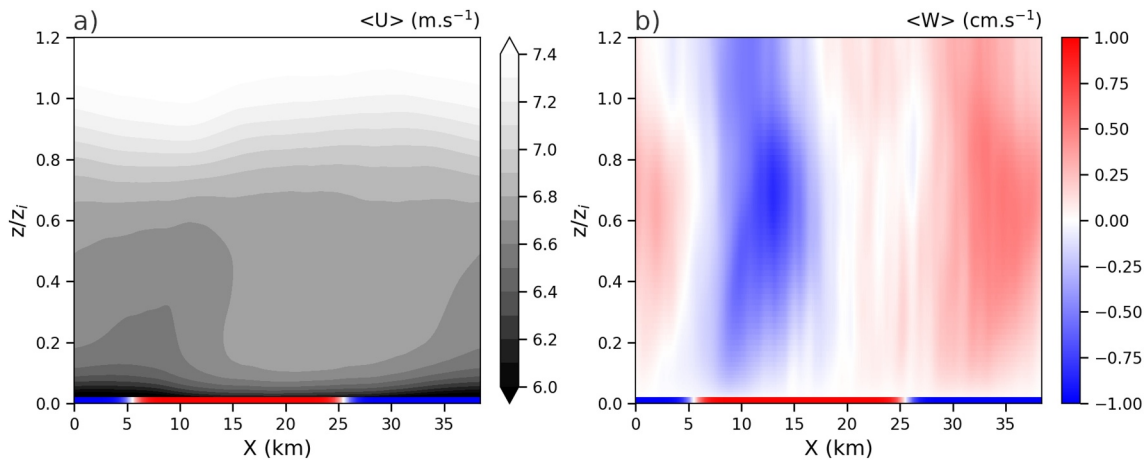


Figure 4. Vertical cross-section of (a) mean zonal wind and (b) vertical velocity. Note the change in units of the vertical velocity compared to instantaneous fields (Figure 2). The altitude is normalized by the domain mean height of the atmospheric boundary layer, $z_i = 600$ m.

the flux profile at $X = 11.5$ km (Figure 3b) shows a concave shape from the surface to $z/z_i = 0.7$ together with a maximum of entrainment at $0.9z_i$. This shape is a consequence of the “thermal overshoot”, which will be discussed in Section 4.4.3. Humidity profiles (not shown) show that the ABL moistens when crossing the front. At $X = 11.5$ km, the lower ABL dries out while the upper ABL continues to moisten consistently with the vertical gradient of moisture flux $\langle w.r_v \rangle$ (not shown) positive from the surface up to $0.7z_i$ associated with rising moist updrafts.

Figure 4 shows that the zonal wind increases approximately 5 km downwind of the cold to warm front. A subsidence is evident from $X = 7$ km to $X = 17$ km and we will investigate this in the following. Over warm water, the zonal wind increases (Figures 3c and 4a): the wind profile at $X = 23$ km matches Ref W (red dashed profile), that is, a well ML with constant wind speed of magnitude ≈ 6.7 m.s^{-1} , up to $z/z_i = 0.65$. Over the end of the cold SST (at $X = 4$ km), the wind profile is more sheared than elsewhere and does not collapse with Ref C (blue dashed profile). The fact that the ABL matches Ref W at the end of the warm zone but that it does not align with Ref C at the end of the cold zone is a direct consequence of the length of the domain and the cyclic condition. At the cold to warm SST front, the ABL is destabilized by the increase of SST. The increased convective activity (described later in Section 4.4) efficiently mixes the entire ABL depth on a distance less than the length of the warm patch. At the warm to cold front, the decrease of SST stabilizes the ABL. The ABL response is much slower than for the other front, as noted by S20 in their Es2 simulation. The ABL would need a distance greater than the length of the cold zone to reach an equilibrium on its full depth with the colder SST. As a consequence, we observe a more sheared profile in mean wind and nonlinear flux at $X = 8.5$ km compared to the homogeneous simulation Ref C. The momentum flux profiles (Figure 3d) also show a nonlinear profile with Z at $X = 8.5$ km and $X = 11.5$ km at the location of the “thermal overshoot.” In contrast, reference profiles have $\langle uw \rangle$ profiles almost linear with height. By $X = 23$ km, the momentum flux profiles are similar to Ref W. The link between the mean wind and the structure of the ABL will be further discussed in Section 4.4.

Surface fluxes are shown in Figure 1. Both sensible and latent heat fluxes follow closely the SST jump. Note, however, that the latent heat flux shows a second increase at $X = 8.5$ km that is mainly due to the difference of the mixing ratio at $z = 1$ m from its saturation value. The increase of the normalized friction velocity is also more progressive throughout the front.

4.2. The U Budget

To understand the spatial evolution of the mean wind and particularly the processes at stake in the lower layer wind acceleration, the dominant terms of the Lagrangian zonal momentum budgets (Equation 3) are shown in Figure 5. This follows the analysis of Redelsperger et al. (2019) who used advected boxes to compute their budget terms, capturing nonstationary processes over a heterogeneous surface.

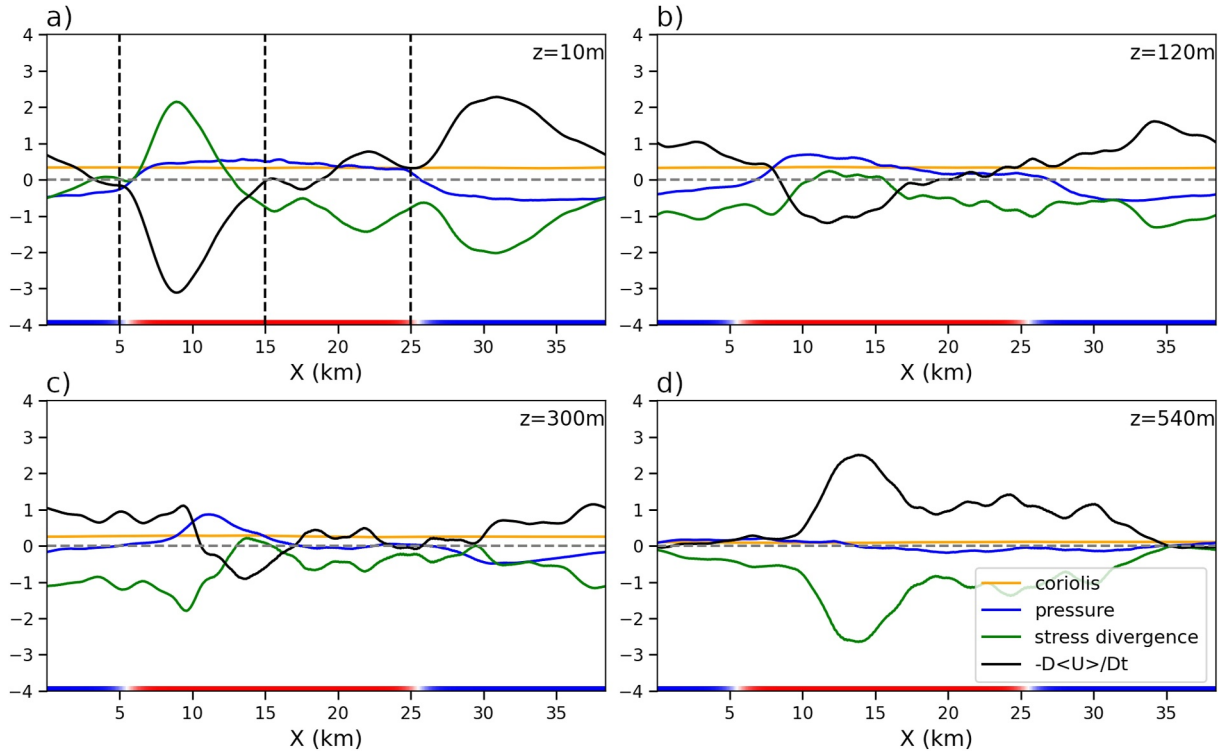


Figure 5. Zonal momentum budget terms (10^{-4}m.s^{-2}) from Equation 3: (a) at 10 m near surface, (b) at the bottom of the mixed layer ($z = 0.2z_i = 120$ m), (c) at the middle of the atmospheric boundary layer ($z = 0.5z_i = 300$ m), and (d) at the top of the boundary layer ($z = 0.9z_i = 540$ m). Only dominant terms are represented. The term $D\langle U \rangle /Dt$ is the total time derivative: $D\langle U \rangle /Dt = \partial\langle U \rangle /\partial t + \langle U \rangle \partial \langle U \rangle /\partial x$. The colored line at the bottom of each graph represents the sea surface temperature as in Figure 2.

The Lagrangian wind response at the surface can be split into three phases (black line in Figure 5a). From 5 to 15 km, the flow accelerates, reaching a peak at $X = 8.5$ km. From $X = 15$ km to $X = 25$ km, the flow decreases despite the surface air still being warmed by the SST (solid black line in Figure 1a). Finally, over the cold SST, the flow decelerates more rapidly than in the previous phase. Above the surface layer (SL), at the bottom of the ML ($z = 120$ m), the zonal wind budget shows similar behavior but with lower intensity and more advected downwind. In the upper layers, U slows down everywhere with the most significant reduction around $X = 13$ km. The dominant term explaining the Lagrangian evolution of the zonal wind is the turbulent Reynolds stress. The magnitude of the pressure term also varies along the X direction. Compared to the other terms, it is negligible at the top and bottom of the ABL but not in the middle. For SST fronts at the mesoscale, pressure and Reynolds stress terms have been related to the PA and DMM mechanisms, respectively. In Figure 5, the stress divergence term dominates the pressure gradient term, hence the DMM mechanism is the main mechanism.

4.3. Consequences of the DMM Mechanism

In the case of mesoscale SST fronts, the consequences of the DMM and PA mechanisms are linear relations between wind, stress, and SST based on observations (O'Neill et al., 2012), reanalysis (Desbiolles et al., 2023), and analytical models (Ayet & Redelsperger, 2019). These relations were derived for gradients of SST one order of magnitude smaller than the present SST gradient. For the DMM, the two relations involve the 10 m wind (U_{10}) divergence or surface stress (τ) and the along-wind SST gradient. In our across-front configuration, they read

$$\partial_x U_{10} = \alpha_{DMM,U} \frac{dSST}{dx} \quad (5)$$

$$\partial_x \tau = \alpha_{DMM,\tau} \frac{dSST}{dx} \quad (6)$$

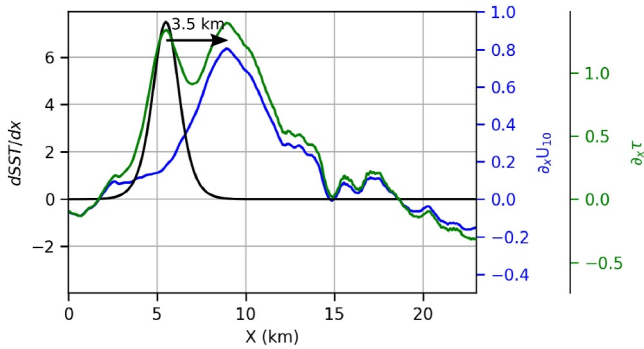


Figure 6. Ten meter wind divergence (10^{-5} , s^{-1} blue line), wind stress divergence (10^{-6} , $N.m^{-3}$ green line) above the cold to warm front in S1. The sea surface temperature gradient is the black line (10^{-4} , $K.m^{-1}$).

Figure 6 shows 10 m wind divergence (solid blue line) when crossing the cold to warm front (SST in black) from the S1 simulation. Wind divergence is similar to the SST gradient when shifted by 3.5 km with a strong peak correlated to the SST gradient peak. This peak is wider than the SST gradient peak, which shows that the surface wind response to the SST increase is not instantaneous.

The surface stress divergence (green line) shows a similar peak 3.5 km after the maximum SST gradient. It also shows a second response located above the maximum SST gradient (from $X = 4$ km to $X = 6$ km), which is not observed in $\partial_x U_{10}$. Based on the bulk formulation of the fluxes ($\tau = C_d U_{10}^2$, C_d the drag coefficient), we propose the following hypothesis: the first response of $\partial_x \tau$ arises from a stability effect on the drag coefficient, while the second response results from the changes in U_{10} . Note that the surface latent heat flux also shows a similar behavior (Figure 1d).

These observations translate into a spatial correlation between the divergence of mean wind at 10 m height and the gradient of SST which shows a maximum of 0.78 for a lag of 3.55 km. The correlation between the stress divergence and SST gradient reaches its maximum at 0.62 for a lag of 3.5 km, but a second peak is observed at 0.49 for a lag of 0 km. These correlations are lower than those over mesoscale SST fronts. This low score results from the slope difference between SST gradient and wind divergence as well as the second peak in wind stress divergence.

To compare against the literature, we performed linear regressions between the SST gradient and the shifted (by 3.5 km) signal of wind or stress divergence. The regression coefficients are $\alpha_{DMM,U} = 0.0268 \text{ m.s}^{-1} \cdot K^{-1}$ and $\alpha_{DMM,\tau} = 0.00054 \text{ N.m}^{-2} \cdot K^{-1}$. Both coefficients are one order of magnitude lower than the literature: Desbiolles et al. (2023) found $\alpha_{DMM,U} = 0.12 \text{ m.s}^{-1} \cdot K^{-1}$ for similar background wind speed whereas O'Neill et al. (2012) found values of $\alpha_{DMM,\tau}$ ranging from $0.012 \text{ N.m}^{-2} \cdot K^{-1}$ to $0.022 \text{ N.m}^{-2} \cdot K^{-1}$ in different regions. The PA mechanism, characterized by a linear relation between ABL-integrated wind divergence and SST laplacian at the mesoscale, is not observed here: the correlation between ABL-integrated wind and the laplacian of SST is 0.18 at best.

We find that at submesoscale, mesoscale relations associated with the DMM mechanism do not directly apply because: (a) the maximum of correlation between wind divergence and wind stress divergence is shifted due to advection by 3.5 km and (b) the linear regression coefficients are one order of magnitude lower. The wind stress divergence also exhibits a second peak of high correlation with no lag: it results from the instantaneous response of the stability coefficient in the surface wind stress bulk formula.

4.4. Coherent Structure Analysis

We now focus on understanding the processes driving DMM over warm SST by describing the turbulent contribution to the U budget. We decompose the flow into coherent structures identified by the conditional sampling C10 (see Section 3.2). This enables the decomposition of the mean flux with contributions from each coherent structure.

4.4.1. Life Cycle of a Pair of Plumes

To illustrate the typical instantaneous structure of turbulence, we show slices (in the Y direction) of coherent structure and humidity. Figure 7 shows turbulent object detected by the conditional sampling and the associated humidity anomaly at two different times of their lifetime (a 13 min interval). The slices are shifted in the X direction from $X = 12.9$ km to $X = 16.9$ km, assuming advection by the vertically integrated wind U_{adv} (from surface to $z_i = 600$ m), $U_{adv} = 6.53 \text{ m.s}^{-1}$.

The snapshots in Figure 7 illustrate the development of two updrafts on the warm SST after the SST front. We recall that we emit two tracers at the surface, depending on the SST. On cold SST, we emit tracer 1 and objects detected from this tracer are in red (for updrafts) and purple (for subsiding shells). On warm SST (for X between 5 and 25 km), we emit tracer 2, with objects in orange (for updrafts) and pink (for subsiding shells). A third tracer,

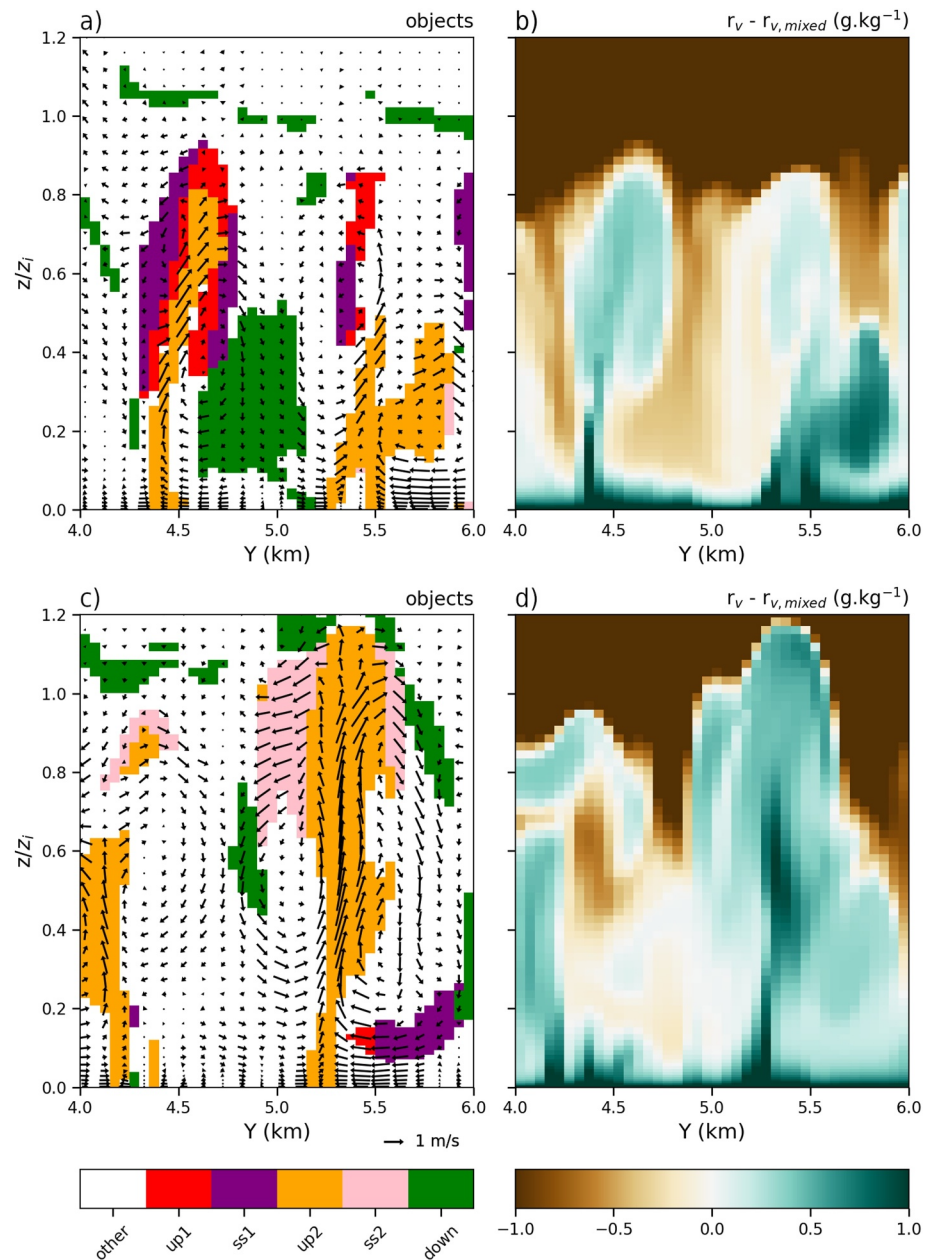


Figure 7. Slices of the S1 simulation: (a and b) at $(t, X) = (2 \text{ hr } 29 \text{ min } 30 \text{ s}, 12.1 \text{ km})$ and (c and d) at $(t, X) = (2 \text{ hr } 42 \text{ min } 30 \text{ s}, 16.9 \text{ km})$. They describe the same object but at different instants, advected by the ABL-averaged velocity U_{adv} . Panels (a) and (c): coherent structures as detected by C10 in color and wind fluctuations vector field. Acronyms in the object label are “up” for updrafts, “ss” for subsiding shells, “down” for downdrafts with numbers corresponding to the tracer emitted on cold (1) and warm (2) water. Panels (b) and (d): humidity anomaly with respect to $r_v - r_{v,mixed}$, the mixed-layer water vapor mixing ratio. Please note that when tracer 1 and 2 are present at the same location, the conditional sampling uses the most concentrated one.

with objects in green, is emitted above the ABL the same way on cold and warm SST. The labels for objects read: “up” are updrafts, “ss” are subsiding shells, “down” are downdrafts and “other” is the rest of the flow. The slices of Figure 7 are at positions where tracer 2 is already emitted from the surface, and where tracer 1 is still present in the atmosphere aloft (it has not yet dissipated). It illustrates the onset of turbulence after the front.

In Figure 7a, two growing plumes can be seen. At $Y = 4.5 \text{ km}$, a developing updraft with tracer 2 enters residue of tracer 1. This updraft carries a positive anomaly of humidity from the surface to the upper layers of the ABL with homogeneous values in the hat of the mushroom-shaped object (Figure 7b). At $Y = 5.5 \text{ km}$, a new updraft is

formed with only tracer 2. The large patch of green at around $Y = 4.75$ km and from $0.1z_i$ to $0.5z_i$ is a dry tongue (Couvreur et al., 2007), and it is detected as a downdraft.

Thirteen minutes later, the same plumes have extended vertically in the ABL (Figures 7c and 7d). They are almost exclusively carrying tracer 2. Tracer one objects (“up” and “ss”) are still present (e.g., at $Y = 5.5$ km) but are remnants of inactive plumes that also carry a positive anomaly of humidity. Even though the inversion is weak (as defined in Sullivan et al. (1998)), the updraft at $Y = 5.2$ km diverges at the top of the ABL, inducing downward motion with subsiding shells streaming down the plume. In between the updrafts (from $Y = 4.3$ km to $Y = 5$ km), we observe a dryer zone with no clear structure associated: a small downdraft is detected at $Y = 4.9$ km and $Z = 0.6z_i$ but it does not cover the wide gap between the two updrafts. This dryer air is also an intense downward motion (about 0.5 m.s^{-1}).

The conditional sampling method detects updrafts where the humidity anomaly is the strongest: at $Y = 5.2$ km, the trunk of the mushroom-shaped updraft is surrounded by nonturbulent air (labeled “other” in Figure 7c), but this surrounding air still has a positive anomaly of humidity (Figure 7d, especially visible on the right of the trunk). Whether these objects are a consequence of lateral entrainment, the wake of the rising plume or another process deserves further investigation with a higher resolution simulation.

After describing what instantaneous structures look like, the next sections quantify the mean contribution of those turbulent structures to different mean quantities.

4.4.2. Strong Thermals Near the Front

This section focuses on the increase of the 10 m wind at $X = 8.5$ km as seen in the U budget (Figure 5a). This altitude belongs to the SL defined as the lower 10% of the ABL. We use two diagnostics to sample the flow conditionally: one in the SL and another in the ML.

The stability of the ABL influences the SL structure (D. Li & Bou-Zeid, 2011; Q. Li et al., 2018; Salesky et al., 2017). Salesky et al. (2017) showed that the SL structure and the transport of momentum and scalars can be quantified by an efficiency metric based on a quadrant analysis. The quadrant analysis uses the signs of the fluctuations to define four quadrants for each flux. The efficiency metric is defined as the ratio of the total flux over the down-gradient flux contributions. For momentum flux, the down-gradient flux contributions are computed by averaging over quadrants 2 ($\tilde{u} < 0$ and $\tilde{w} > 0$) and 4 ($\tilde{u} > 0$ and $\tilde{w} < 0$). These correspond to upward (ejections) and downward (sweeps) motions, respectively. A high efficiency corresponds to a minimal up-gradient transport (ejections and sweeps are dominant), whereas low efficiency corresponds to similar up and down-gradient transports.

In our study, the ABL transitions from weakly unstable over cold SST to moderately unstable over warm SST. Figure 8 illustrates the efficiency of momentum transport on the resolved flow for $z < 0.3z_i$. At $X = 8.5$ km, the efficiency is similar to that at $X = 4$ km. Further down the front, efficiency decreases (from ~ 0.9 at $X = 8.5$ km to ~ 0.8 at $X = 23$ km), resulting in less momentum being injected into the ABL interior.

Within the ML, we now apply the conditional sampling described in Section 3.2 to detect coherent structures. At $X = 8.5$ km, the buoyancy of the updrafts is similar to that at $X = 23$ km (Figure 9a) and their conditionally averaged vertical velocity increases rapidly as they cross the cold to warm front (Figure 9b). This rapid response can be explained as follows: updrafts are initiated with warm, moist air from the surface and they transport these quantities inside the ML. In contrast to the rest of the flow which has not yet been influenced by the warmer SST, this establishes large positive temperature and moisture anomalies, inducing an increase in buoyancy within updrafts.

From $X = 4$ km to $X = 8.5$ km, the combined effect of strong updrafts and a SL structure that efficiently transports surface quantities are extracting momentum from the surface. At the surface, the U wind is slower, so the SL injects slower winds upwards (Figure 9c; \tilde{u}_{up} at $X = 8.5$ km is lower by 10 cm.s^{-1} than at $X = 23$ km and $z/z_i = 0.1$). This leads to a negative extremum of -1.30 in the normalized mean momentum flux profile at $X = 8.5$ km (Figure 3c dashed black line) and so a positive contribution ($-\partial <uw>/\partial z > 0$) in the U budget from 0 to $0.15z_i$ and so a wind increase.

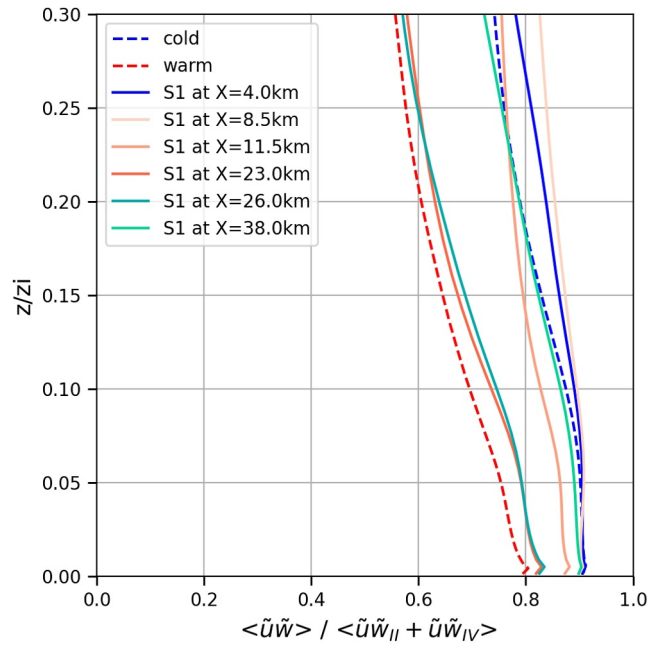


Figure 8. Efficiency of momentum transport using a quadrant analysis of the resolved flow in the S1 simulation (full line) and in the reference simulations (dashed lines). In the figure label, quadrants are defined as $\tilde{u}\tilde{w}_{II} = \{\tilde{u}\tilde{w}, \tilde{u} < 0 \text{ and } \tilde{w} > 0\}$ and $\tilde{u}\tilde{w}_{IV} = \{\tilde{u}\tilde{w}, \tilde{u} > 0 \text{ and } \tilde{w} < 0\}$.

However, caution is needed when interpreting these results because: (a) the total flux, obtained from the contribution of the structures identified with the conditional sampling, does not present a minimum in $\langle u w \rangle$, and (b) the SL is poorly resolved, with 15 vertical grid points, which raises concerns about the reliability of the quadrant analysis in this layer.

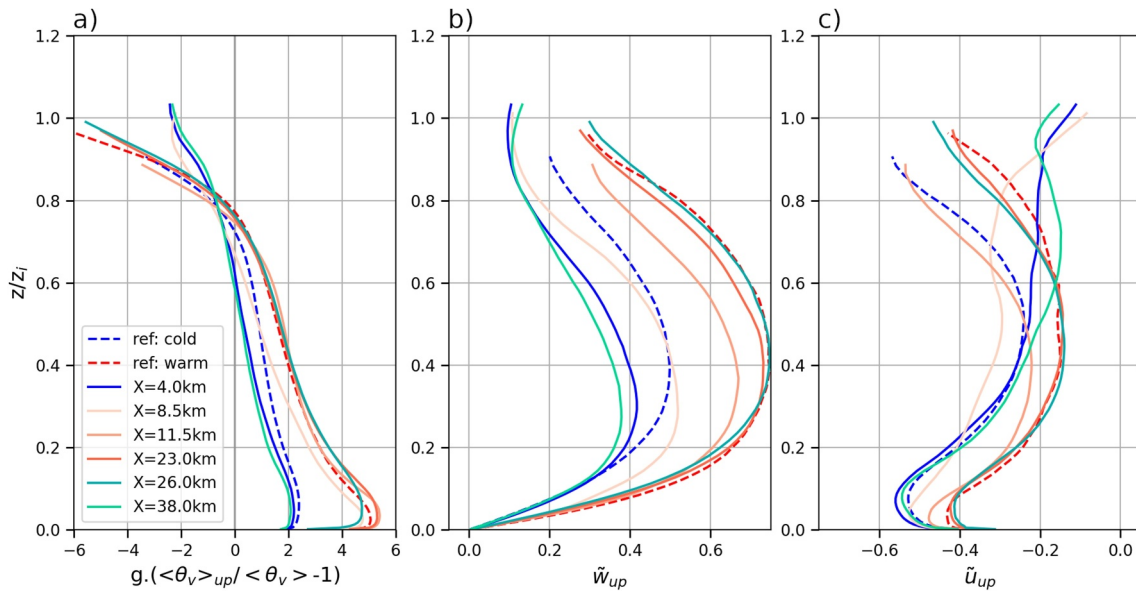


Figure 9. Updraft characteristics with objects detected by C10 conditional sampling. Full lines for S1 simulations and dashed lines for the reference simulations. Profiles are plotted only if the areal fraction of updrafts is greater than 5%. (a) Buoyancy (10^{-3} m.s^{-2}), (b) resolved fluctuations of vertical wind: $\tilde{w}_{up} = \langle W \rangle_{up} - \langle W \rangle$ (m.s^{-1}), (c) same as (b) but for the fluctuations of U (m.s^{-1}).

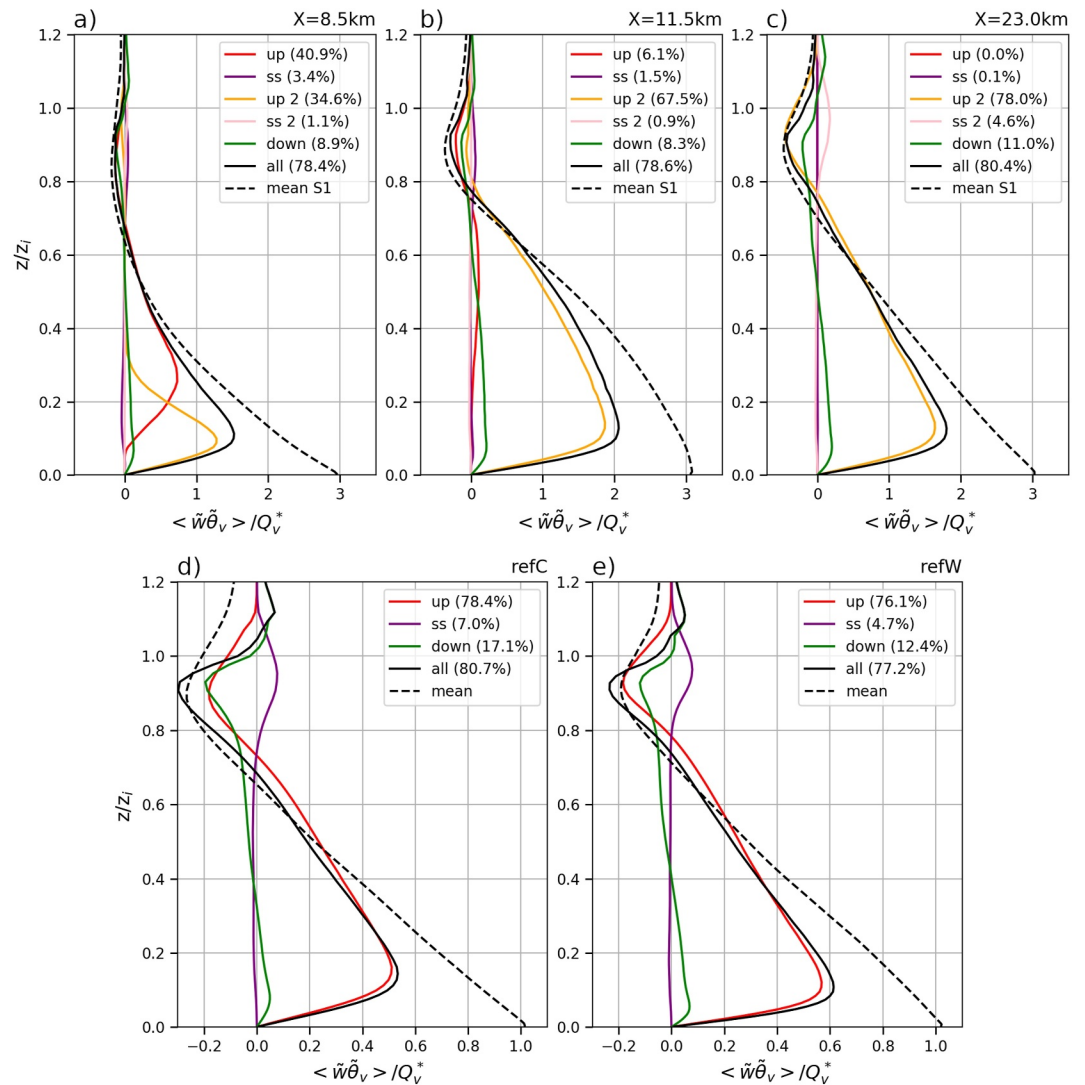


Figure 10. Vertical buoyancy turbulent flux profiles with the contribution of different coherent structures (the percentage next to the name of the structure is the vertically integrated contribution to the flux defined as in Table 2: “up” are updrafts, “ss” are subsiding shells, “down” are downdrafts. The structures associated to surface tracer emitted on the cold (warm) surface are “up” and “ss” (“up2” and “ss2”), respectively. First row: profiles from S1 at (a) $X = 8.5$ km, (b) $X = 11.5$ km and (c) $X = 23$ km. Second row: profiles from the reference simulations: (d) RefC and (e) RecW.

Updrafts react faster than the rest of the flow when crossing the front. Their increased buoyancy enhances their vertical velocity and also transports surface properties in the ABL interior: moist air with slow winds is injected into the ABL.

4.4.3. The “Thermal Overshoot”

The intense updrafts described previously are advected by the mean wind and continue to ascend. By $X = 11.5$ km, they reach the top of the ABL and overshoot, entraining dry and warm air into the boundary layer. When examining the contribution of each coherent structure to the buoyancy flux, they account for about 80% of the total flux (Figure 10). Updrafts are dominant over the entire depth of the ABL. In the entrainment zone (from $z/z_i = 0.8$ to $z/z_i = 1.1$), they are still contributing to most of the flux but downdrafts also play a role in setting the vertical minimum of buoyancy flux. The entrainment rate can be approximated at first order by this minimum (Sullivan et al., 1998), and it is maximum at $X = 11.5$ km. At this location, the entrainment velocity is $2.27 \text{ cm}\cdot\text{s}^{-1}$, which is between the values from RefW ($2.49 \text{ cm}\cdot\text{s}^{-1}$) and RefC ($1.71 \text{ cm}\cdot\text{s}^{-1}$). After the “thermal overshoot,”

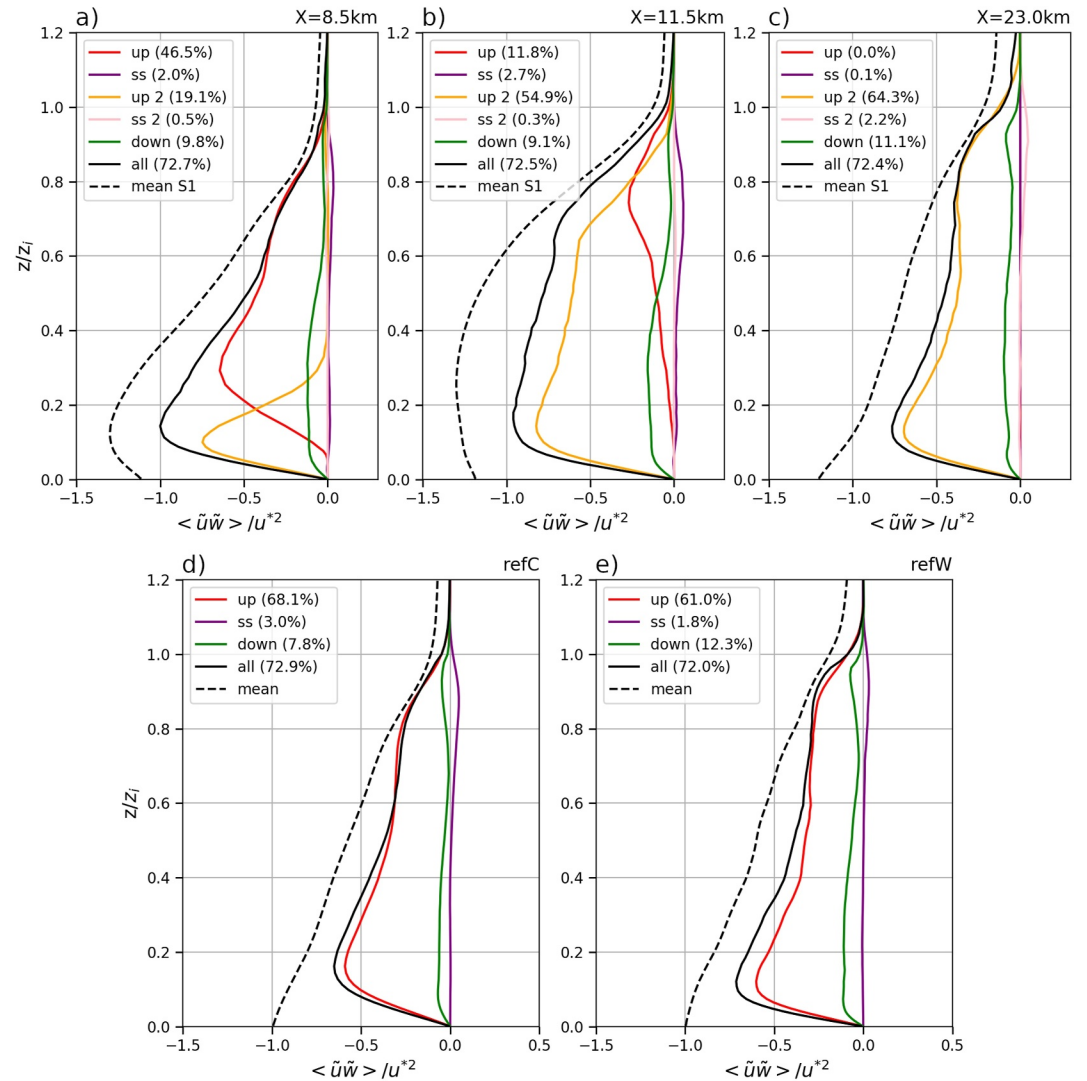


Figure 11. Same as Figure 10 but for the momentum flux.

entrainment rates for S1 drop to values lower than the entrainment velocity in RefC (not shown). We identified that both updrafts and downdrafts (Figure 10) are the coherent structures responsible for the entrainment of above-ABL air into the ABL interior. Figure 7 shows that the updrafts also create rotational motion at their periphery, which could induce the transport of dry and warm air. However, this is not detected as “downdraft” by the conditional sampling, making it unclear whether the updrafts induce other processes that influence the entrainment at the top of the ABL. This entrainment induces an ABL height change of 50 m, which is 10 times less than the one observed by Yang et al. (2024) near the Kuroshio extension although they measured a submesoscale SST gradient of $0.36^\circ\text{C}\cdot\text{km}^{-1}$, which is less intense than our gradient ($1.5^\circ\text{C}\cdot\text{km}^{-1}$).

In the lower layers of the ABL, $DU/Dt > 0$ (Figure 5b). At $X = 11.5$ km and $z = 120$ m ($0.2 z_i$), the turbulent term in the U budget acts as a source consistent with the negative vertical gradient of the turbulent momentum flux $\langle uw \rangle$ below $0.4 z_i$ (Figure 11b, dashed line). This behavior contrasts with the constant positive gradient of the flux observed in the reference simulations (Figures 11d and 11e).

Turbulent coherent structures cannot explain this negative gradient. They contribute with a positive gradient to the mean flux (Figure 11b, solid black line). These structures explain 72% of the mean momentum flux at $X = 11.5$ km. Other potential candidates that might explain the increased wind in the lower ABL were explored in Section 4.4.1. Instantaneous slices of the object show that the C10 conditional sampling does not capture the

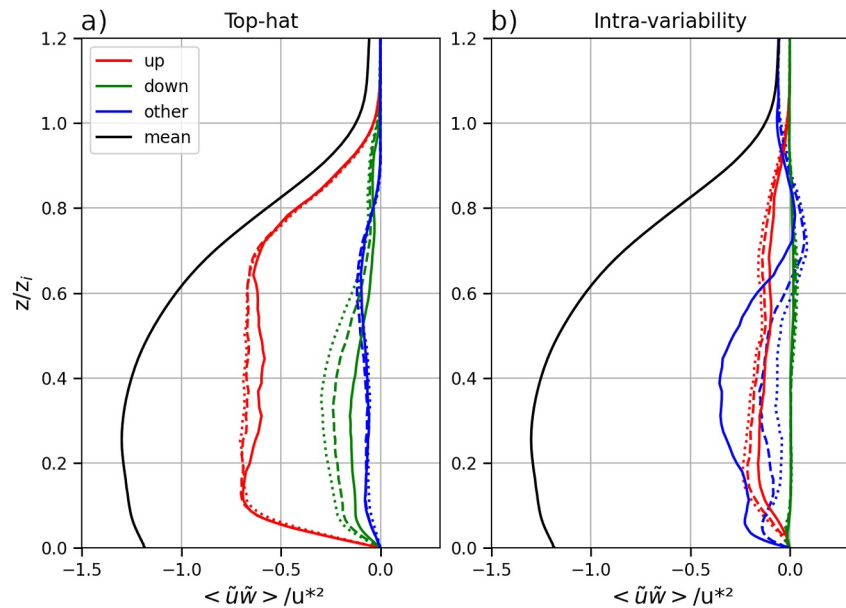


Figure 12. (a) Top-hat and (b) intra-variability decomposition for the resolved turbulent momentum flux with varying values for m for C10 conditional sampling and at $X = 11.5$ km in S1: full line $m = 1$, dashed line $m = 0.5$ and dotted line $m = 0.25$. “up,” “down,” and “other” being disjoints categories and their surface coverage summing to 1, the sum of the top-hat part and the intra-variability part of all objects for a selected m is equal to the mean resolved flux (in black full line).

downward motion between the two updrafts (Figure 7c). This suggests that some structures may not be turbulent enough to be detected by the method used here, or that no top-ABL tracer is transported by these structures. Consistently, we also observe that the mean vertical wind is negative and locally increases around $X = 11.5$ km (Figure 4b).

To confirm this hypothesis, we further decompose the entire flow into top-hat and intra-variability contributions. In Figure 12 (solid lines), the main contribution comes from the top-hat part of the updrafts and the intra-variability of “other.” The latter is of particular interest as it exhibits a negative vertical gradient from the surface up to $z/z_i = 0.5$ (and so a U acceleration). The fact that this signal is labeled as “other” (i.e., it does not belong to any coherent structure of Figure 11b at $X = 11.5$ km) indicates that the underlying objects are not turbulent enough to be detected by C10. The label “intra-variability” suggests that it represents local mixing. A sensitivity study on the intensity of the filtering process (the m parameter in Equation 2 of Couvreux et al. (2010)) was conducted with results shown in Figure 12. When m is decreased (capturing air that is less turbulent), the signal that is detected as local mixing of “other” is then identified by C10 as “downdraft,” and with the top-hat decomposition, it is labeled as nonlocal contribution. These results show that the interpretation of the top-hat decomposition depends significantly on how the objects are defined in the first place as already noted by Wang and Stevens (2000).

At $X = 11.5$, or 6.5 km downwind of the front, strong updrafts overshoot, and a maximum of entrainment is observed. In the lower part of the ABL, the zonal wind is accelerated by less turbulent subsiding air, which acts like a compensating subsidence, transporting momentum from the top of the ABL to the lower layers.

4.4.4. Mixing Far From the Front

At the end of the warm SST patch (from $X = 18$ km to $X = 23$ km), the ABL has a convective ML with almost constant wind and temperature from 0.15 to $0.7z_i$ (Figures 3c and 3a). The local ABL height remains constant. Coherent structures, sampled with C10, represent most of the mean momentum flux (73% at $X = 23$ km, Figure 11c) and buoyancy flux (80% at $X = 23$ km, Figure 10) with a primary contribution from updrafts.

With a positive gradient of the flux, turbulence acts as a drag, balancing the Coriolis term and the pressure gradient term in the lower layers of the ABL (Figures 5a and 5b). This drag primarily results from the updrafts that inject slow winds from the surface into the ABL. As discussed in Section 4.4.2, slow winds (Figure 9c) is

extracted from the surface but less efficiently here (Figure 8), as the SL structure had time to adjust to the SST change.

Far from the positive SST jump, the mean wind (Figure 3c), mean temperature (Figure 3a), mean flux as well as their decomposition (Figures 10c and 11c) are very similar to the profiles from RefW (Figures 10e and 11e) with the majority of the momentum flux being explained by updrafts (64% in S1, 61% in RefW) followed by downdrafts (9% in S1, 12% in RefW). Although the temperature shows close similarities with the reference simulations, the zonal wind profile is more sheared in S1, at all X except at the end of the warm zone, than in RefC or RefW. This shear is a consequence of the cyclic condition used for the east and west boundaries: after the warm to cold transition, reaching an equilibrium for the full depth of the ABL would require more downfront distance than the length of our cold SST zone. In fact, a stable internal boundary layer grows from $X = 25$ km and onward.

By the end of the warm SST zone, the ABL has returned to a quasi-equilibrium state of a growing convective boundary layer.

5. Discussion

The analysis showed that in our simulation, the response of the atmosphere to the SST gradient is akin to the DMM mechanism: (a) the mean budget analysis shows that wind changes are primarily driven by turbulent mixing (b) we observe a strong, delayed, correlation between SST gradient and the wind divergence at 10 m with the highest correlation occurring at a lag of 3.5 km. This lag reflects the effect of advection, which, similar to Lambaerts et al. (2013) and Ayet and Redelsperger (2019), delays the response of the ABL. The pressure gradient term is not negligible in our case, but there is no significant delayed correlation between the wind gradient and the laplacian of SST (the PA mechanism). The ABL response is consistent with previous studies (Foussard et al., 2019; Kilpatrick et al., 2014; Lambaerts et al., 2013), given that we are in a strong wind configuration ($7.5 \text{ m}\cdot\text{s}^{-1}$). Although the correlations for 10 m wind divergence and stress divergence with along-wind SST gradient are high, they are not comparable to the correlations in other studies, conducted over several SST fronts. Even though the ABL remains in a convective regime, the flow structure evolves from roll to a mixed cell-roll state. This transition of the turbulent structures may explain why the flow needs more time to adjust to the SST change. Investigation of the influence of the turbulent transition on the ABL response timescale is left for further study. The regression coefficients $\alpha_{DMM,U_{10}}$ and $\alpha_{DMM,\tau}$ are one order of magnitude smaller than those found in the literature for both the relations between stress divergence and SST gradient (Foussard et al., 2019; O'Neill et al., 2012; Plagge et al., 2016) and wind divergence and SST gradient (Ayet & Redelsperger, 2019; Foussard et al., 2019; Plagge et al., 2016). This difference may result from both advection (which is stronger at these small scales) and nonlinear effects on the turbulent stress over the ABL (e.g., internal boundary layer growth and coherent structures), whose shape is crucial for explaining the regression coefficient (Ayet & Redelsperger, 2019).

In the case of weak surface winds and a strong SST front, Redelsperger et al. (2019) argued that changes in the stability of the SL play a key role in setting the turbulent fluxes through the drag coefficient. In our simulation, we used momentum efficiency as a proxy to quantify structural changes in the SL, and by extension, changes in stability. Near the front, we observed that changes in stability induced by the front altered the momentum transport (the fluxes) from the SL into the ABL. This was due to a combined change in SL turbulence and of coherent structures (updrafts) inside the ABL. However, we also observed an increase in surface fluxes farther from the front. We recall here the general form of bulk formulas for surface flux: for momentum $u^*w^* = C_D U^2$ and for a scalar $w^*s^* = C_s U \Delta S$ where ΔS the difference between the surface value and the value at first model level. We suggest that the initial increase is due to changes in stability coefficient in the bulk formulas (i.e., C_D and C_s), whereas the second increase results from resolved motions, specifically the enhanced compensating subsidence, which influences surface flux computations through the terms U and ΔS in the bulk formulas.

This is consistent with continental convection results of Koning et al. (2021) which show that surface fluxes play a crucial role in initiating convection, which in turn influences surface fluxes.

In the S1 simulation, the difference between extrema of z_i is 50 m along the X dimension, while S20 observed a maximum difference of z_i of 60 m. Although S20 used a proper inflow boundary condition and we used cyclic conditions, the change in boundary layer height along the SST gradient is similar. This evolution of z_i along X aligns with other idealized studies (Kilpatrick et al., 2014; Samelson et al., 2006; Watanabe et al., 2022).

However, in a more realistic context, Redelsperger et al. (2019) found that the ABL height remained constant when crossing the front. It is unclear whether the entrainment processes are explicitly resolved, as 50 m at the altitude of z_i corresponds to approximately four vertical levels in our simulation, which may not be sufficient (Sullivan et al., 1998). Note that the S1 simulation does not produce any clouds at the overshoot despite the use of a condensation scheme. Under different atmospheric conditions, the intense thermals could trigger shallow convection (Desbiolles et al., 2021; Watanabe et al., 2022) and could further impact the ABL height.

We conducted an object-oriented analysis that provides insights on the structure of the turbulent ABL. Wein-kaemmerer et al. (2023) and Brient et al. (2024) used the C10 conditional sampling to describe heat and moisture transport by coherent structures whereas we used it to examine the transport of both buoyancy and momentum. The structures described by Brient et al. (2024) in their dry continental convection case and the S1 simulation are similar (not shown): lines of convergence at the surface merge to form mushroom-like objects, surrounded by downward-moving air. Updrafts are detected in the core of a wider and positive anomaly of humidity, with subsiding shells streaming down at the edges of the updrafts and downdrafts sparsely populating the space in between them. Although object coverage is similar at all altitudes, the contribution from the subsiding shells and the downdrafts to the latent and sensible heat flux is more significant—especially at the inversion—in their continental case compared to our marine convective case. This may be due to their configuration, which includes both more intense sensible and latent fluxes and a stronger inversion compared to ours. Despite these similarities, our analysis revealed a sensitivity to the threshold used to detect descending structures, which have less contrast with the environment.

The contribution of each object to turbulent fluxes provides a more precise understanding of the DMM mechanism: the general term of “turbulent mixing” can be explained by the combined action of updrafts and enhanced compensating subsidence. Finally, we showed how turbulent structures contribute to the “thermal overshoot,” emphasizing the role played by advection (as analyzed in S20): advection by strong wind influences the instantaneous turbulent structures, and, in turn, these structures contribute to the “thermal overshoot.” Entrainment at the top of the ABL reaches its maximum at the “thermal overshoot,” with the primary contribution from updrafts and a non-negligible contribution from downdrafts. The C10 decomposition revealed that, although the enhanced compensating subsidence is less turbulent than downdrafts, it still exhibits some vertical coherence. Hence, we suggest that if this process was to be taken into account in Cloud Resolving Models, it should be introduced as an additional mass flux term triggered by the underlying SST front.

6. Conclusion

In this study, we simulated an ABL flowing over an idealized submesoscale SST front. We employed a Large Eddy Simulation to resolve most of the turbulent processes.

The zonal mean wind and its budget indicated that, over warm SST, the surface wind increases due to enhanced turbulent mixing, highlighting the importance of the DMM mechanism. The pressure term was found to be less significant, though not negligible, with no observed linear relation between the Laplacian of SST and the integrated wind divergence.

Compared to observations and simulations at larger scales, the correlation between the gradient of SST and the wind divergence is lower. This was found to be a result of the nonlinearities occurring at the submesoscale, which delay the atmospheric response to the SST front.

In order to move beyond the averaged description of the DMM mechanism and to link the averaged and instantaneous structure of turbulence, we investigated the internal structure of the flow using a conditional sampling method. This method identifies coherent structures within the ABL using tracer concentration.

Figure 13 illustrates a conceptual view of the processes at play in the simulation. In the few kilometers after the SST increase, conditional sampling on both instantaneous or mean quantities shows that the intensity of the updrafts (red arrows in Figure 13) increases, whereas the mean wind needs more time to adjust. The flow evolves from a roll to a cell-roll transition state. At first, near surface quantities are efficiently extracted (black arrows in Figure 13) from the SL by updrafts, which inject slow winds and warm moist air into the ABL interior. This leads to an increase in the mean wind at the bottom of the ABL. Next, updrafts carry these quantities throughout the ML. These enhanced updrafts reach the top of the ABL and overshoot the mean ABL height. Examination of the evolution of a convective thermal indicates that, at the overshoot, some of the strongest updrafts diverge and induce downdrafts that entrain air from above the ABL (green arrow in Figure 13). However, the momentum flux

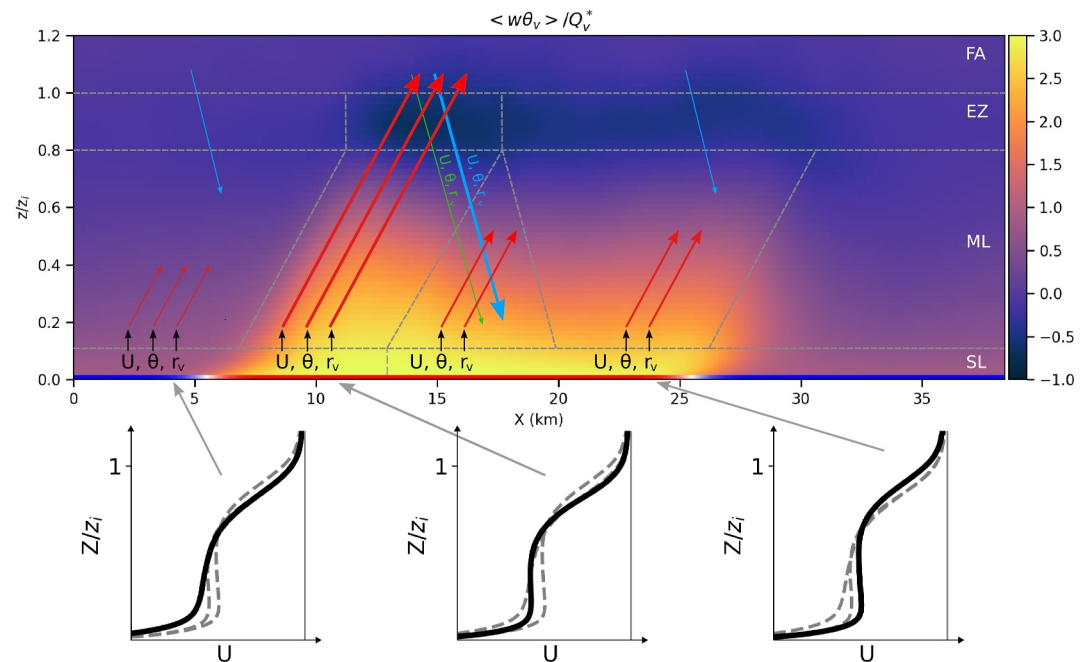


Figure 13. Conceptual view of the different processes in the atmosphere over a submesoscale sea surface temperature front. The background is the total (resolved + subgrid) buoyancy flux normalized by the surface value at $X = 4$ km. The blue and red bar at the bottom of the figure is the SST. Black arrows are quantities transferred from the surface layer to the mixed layer, red arrows are updrafts that transport the quantity from its base up to its top. The green arrows represent downdrafts induced by updraft divergence, and the blue arrows represent compensating subsidence. The width of the arrows indicate the intensity of the transport. EZ is the entrainment zone, FA is the free atmosphere, U is the zonal wind, and θ is the potential temperature and r_v is the water vapor mixing ratio. Below the conceptual view are wind profiles shapes at $X = 4$ km, $X = 11.5$ km and $X = 23$ km. The solid black lines are the profiles at the locations pointed by gray arrows and dashed gray lines are profiles at the other locations.

decomposition showed that they do not transport much wind to the surface. In fact, the default conditional sampling is unable of detecting the structure responsible for the surface wind increase. With a less restrictive object detection, this wind increase and drying of the lower ABL can be attributed to a downward-moving structure, less turbulent than downdrafts, and that we call enhanced compensating subsidence (large blue arrow in Figure 13). Finally, at the end of the warm SST, turbulence acts as a drag force similar to the “cumulus friction” from Dixit et al. (2021). The ABL reaches a quasi-equilibrium, where the mixing by updrafts balances with Coriolis and pressure gradient forces similar to the reference simulation with homogeneous warm SST.

The previous analysis should be generalized to other environmental conditions that are more realistic. In particular, we expect that changes in the strength of the inversion at the top of the boundary layer could induce other types of downward structures. For instance, a weaker inversion is expected to increase entrainment by folding more air from above the ABL into updrafts (Sullivan et al., 1998), whereas stronger inversion could enhance updraft divergence at the ABL top and induce more turbulent downdrafts (Brient et al., 2024). We studied a highly idealized configuration with across-front winds. In a more realistic configuration, we expect that the ABL response to SST changes will be a combination of DMM and PA and that this combination will depend nonlinearly on the wind direction relative to the SST front. Additionally, a moister environment could lead to cloud formation, and the presence of cumulus may modify the intensity of the exchange between the free troposphere and the boundary layer. Although the SST gradient used here ($1.5^\circ\text{C}\cdot\text{km}^{-1}$) is already strong, stronger contrasts, such as those encountered over the transition from sea-ice to sea in polar regions (Fogarty et al., 2024; Watanabe et al., 2022; Wenta & Herman, 2018) should be analyzed in further studies. Finally, our analysis is a first step toward exploring the imprint of SST fronts in the ABL in synthetic aperture radars (SAR) data. Indeed, Ayet et al. (2021) showed how SAR images (in which instantaneous changes of surface wind appear) above an SST front show wind structures that resemble that of an LES. The coherent structure analysis of this paper could hence be applied to more realistic LES and compared to SAR images to help decipher this high resolution data.

Data Availability Statement

Data outputs from the simulations are available on a Zenodo archive (Part 1: Jacquet et al. (2024a), Part 2: Jacquet et al. (2024b)). Post-process scripts as well as configuration files to reproduce the simulations can be found in the Zenodo archive (Jacquet et al., 2024c) and on this repository (https://github.com/HugoJacq/ABL_response_to_SST_front). Zenodo archives are licensed under Creative Commons Attribution 4.0 International and the scripts on the GitHub repository are licensed under MIT.

Acknowledgments

We thank the MesoNH support team for their help in producing the simulations. HJ was funded by the MEDIATION project, managed by the Agence Nationale de la Recherche for France 2030 (ANR-22-POCE-0003). HJ, AA, and FC were funded by CNRS MITI grant ALESE. AA was funded by CNES grant TOSCA I-CASCADE and SWOT-POSEIDON. FC acknowledge support from the DEPHY research group funded by CNRS/INSU and Météo-France.

References

- Adrian, R. J. (1996). Stochastic estimation of the structure of turbulent fields. In J. P. Bonnet (Ed.), *Eddy structure identification* (pp. 145–195). Springer Vienna. https://doi.org/10.1007/978-3-7091-2676-9_3
- Ayet, A., Rasclé, N., Chapron, B., Couvreur, F., & Terray, L. (2021). Uncovering air-sea interaction in oceanic submesoscale frontal regions using high-resolution satellite observations. *US Clivar Variations*, 19. <https://doi.org/10.5065/ybca-0s03>
- Ayet, A., & Redelsperger, J.-L. (2019). An analytical study of the atmospheric boundary-layer flow and divergence over an SST front. *Quarterly Journal of the Royal Meteorological Society*, 145(723), 2549–2567. <https://doi.org/10.1002/qj.3578>
- Brient, F., Couvreur, F., Rio, C., & Honnert, R. (2024). Coherent subsiding structures in large eddy simulations of atmospheric boundary layers. *Quarterly Journal of the Royal Meteorological Society*, 150(759), 1–23. <https://doi.org/10.1002/qj.4625>
- Brilouet, P.-E., Bouniol, D., Couvreur, F., Ayet, A., Granero-Belinchon, C., Lothon, M., & Mouche, A. (2023). Trade wind boundary layer turbulence and shallow precipitating convection: New insights combining SAR images, satellite brightness temperature, and airborne in situ measurements. *Geophysical Research Letters*, 50(2), e2022GL102180. <https://doi.org/10.1029/2022GL102180>
- Caniaux, G., Redelsperger, J.-L., & Lafore, J.-P. (1994). A numerical study of the stratiform region of a fast-moving squall line. Part I: General description and water and heat budgets. *American Meteorological Society*, 51(14), 2046–2074. [https://doi.org/10.1175/1520-0469\(1994\)051\(2046:ANSOTS\)2.0.CO;2](https://doi.org/10.1175/1520-0469(1994)051(2046:ANSOTS)2.0.CO;2)
- Christensen, K. T., & Adrian, R. J. (2001). Statistical evidence of hairpin vortex packets in wall turbulence. *Journal of Fluid Mechanics*, 431, 433–443. <https://doi.org/10.1017/S0022112001003512>
- Couvreur, F., Guichard, F., Masson, V., & Redelsperger, J.-L. (2007). Negative water vapour skewness and dry tongues in the convective boundary layer: Observations and large-eddy simulation budget analysis. *Boundary-Layer Meteorology*, 123(2), 269–294. <https://doi.org/10.1007/s10546-006-9140-y>
- Couvreur, F., Hourdin, F., & Rio, C. (2010). Resolved versus parametrized boundary-layer plumes. Part I: A parametrization-oriented conditional sampling in large-eddy simulations. *Boundary-Layer Meteorology*, 134(3), 441–458. <https://doi.org/10.1007/s10546-009-9456-5>
- Cuxart, J., Bougeault, P., & Redelsperger, J.-L. (2000). A turbulence scheme allowing for mesoscale and large-eddy simulations. *Quarterly Journal of the Royal Meteorological Society*, 126(562), 1–30. <https://doi.org/10.1002/qj.49712656202>
- Deardorff, J. W. (1980). Stratocumulus-capped mixed layers derived from a three-dimensional model. *Boundary-Layer Meteorology*, 18(4), 495–527. <https://doi.org/10.1007/BF00119502>
- Desbiolles, F., Alberti, M., Hamouda, M. E., Meroni, A. N., & Pasquero, C. (2021). Links between sea surface temperature structures, clouds and rainfall: Study case of the Mediterranean Sea. *Geophysical Research Letters*, 48(10), e2020GL091839. <https://doi.org/10.1029/2020GL091839>
- Desbiolles, F., Meroni, A. N., Renault, L., & Pasquero, C. (2023). Environmental control of wind response to sea surface temperature patterns in reanalysis dataset. *Journal of Climate*, 36(12), 3881–3893. <https://doi.org/10.1175/JCLI-D-22-0373.1>
- Dixit, V., Nuijens, L., & Helfer, K. C. (2021). Counter-gradient momentum transport through subtropical shallow convection in ICON-LEM simulations. *Journal of Advances in Modeling Earth Systems*, 13(6), e2020MS002352. <https://doi.org/10.1029/2020MS002352>
- Durrán, D. R. (1989). Improving the anelastic approximation. *Journal of the Atmospheric Sciences*, 46(11), 1453–1461. [https://doi.org/10.1175/1520-0469\(1989\)046\(1453:ITAA\)2.0.CO;2](https://doi.org/10.1175/1520-0469(1989)046(1453:ITAA)2.0.CO;2)
- Fairall, C. W., Bradley, E. F., Hare, J. E., Grachev, A. A., & Edson, J. B. (2003). Bulk parameterization of air-sea fluxes: Updates and verification for the COARE algorithm. *Journal of Climate*, 16(4), 571–591. [https://doi.org/10.1175/1520-0442\(2003\)016\(0571:BPOASF\)2.0.CO;2](https://doi.org/10.1175/1520-0442(2003)016(0571:BPOASF)2.0.CO;2)
- Fogarty, J., Bou-Zeid, E., Bushuk, M., & Boisvert, L. (2024). How many parameters are needed to represent polar sea ice surface patterns and heterogeneity? *The Cryosphere*, 18(9), 4335–4354. <https://doi.org/10.5194/tc-18-4335-2024>
- Foussard, A., Lapeyre, G., & Plougonven, R. (2019). Response of surface wind divergence to mesoscale SST anomalies under different wind conditions. *Journal of the Atmospheric Sciences*, 76(7), 2065–2082. <https://doi.org/10.1175/JAS-D-18-0204.1>
- Jacquet, H., Ayet, A., & Couvreur, F. (2024a). Output of simulations for “atmosphere response to an oceanic sub-mesoscale SST front: A coherent structure analysis”: Part 1 [Dataset]. *Zenodo*. <https://doi.org/10.5281/ZENODO.13321540>
- Jacquet, H., Ayet, A., & Couvreur, F. (2024b). Output of simulations for “atmosphere response to an oceanic sub-mesoscale SST front: A coherent structure analysis”: Part 2 [Dataset]. *Zenodo*. <https://doi.org/10.5281/ZENODO.13321834>
- Jacquet, H., Ayet, A., & Couvreur, F. (2024c). Post-process scripts and namlists for “atmosphere response to an oceanic sub-mesoscale SST front: A coherent structure analysis” [Software]. *Zenodo*. <https://doi.org/10.5281/ZENODO.13341467>
- Kilpatrick, T., Schneider, N., & Qiu, B. (2014). Boundary layer convergence induced by strong winds across a midlatitude SST front. *Journal of Climate*, 27(4), 1698–1718. <https://doi.org/10.1175/JCLI-D-13-00101.1>
- Kilpatrick, T., Schneider, N., & Qiu, B. (2016). Atmospheric response to a midlatitude SST front: Alongfront winds. *Journal of the Atmospheric Sciences*, 73(9), 3489–3509. <https://doi.org/10.1175/JAS-D-15-0312.1>
- Koning, A. M., Nuijens, L., Bosveld, F. C., Siebesma, A. P., Van Dorp, P. A., & Jonker, H. J. J. (2021). Surface-layer wind shear and momentum transport from clear-sky to cloudy weather regimes over land. *Journal of Geophysical Research: Atmospheres*, 126(21), e2021JD035087. <https://doi.org/10.1029/2021JD035087>
- Krug, M., Schilperoord, D., Collard, F., Hansen, M., & Rouault, M. (2018). Signature of the Agulhas current in high resolution satellite derived wind fields. *Remote Sensing of Environment*, 217, 340–351. <https://doi.org/10.1016/j.rse.2018.08.016>
- Lac, C., Chaboureaud, J.-P., Masson, V., Pinty, J.-P., Tulet, P., Escobar, J., et al. (2018). Overview of the Meso-NH model version 5.4 and its applications. *Geoscientific Model Development*, 11(5), 1929–1969. <https://doi.org/10.5194/gmd-11-1929-2018>
- Lafore, J. P., Stein, J., Asencio, N., Bougeault, P., Ducrocq, V., Duron, J., et al. (1998). The meso-NH atmospheric simulation system. Part I: Adiabatic formulation and control simulations. *Annales Geophysicae*, 16(1), 90–109. <https://doi.org/10.1007/s00585-997-0090-6>
- Lambaerts, J., Lapeyre, G., Plougonven, R., & Klein, P. (2013). Atmospheric response to sea surface temperature mesoscale structures. *Journal of Geophysical Research: Atmospheres*, 118(17), 9611–9621. <https://doi.org/10.1002/jgrd.50769>

- Li, D., & Bou-Zeid, E. (2011). Coherent structures and the dissimilarity of turbulent transport of momentum and scalars in the unstable atmospheric surface layer. *Boundary-Layer Meteorology*, *140*(2), 243–262. <https://doi.org/10.1007/s10546-011-9613-5>
- Li, Q., Gentile, P., Mellado, J. P., & McColl, K. A. (2018). Implications of nonlocal transport and conditionally averaged statistics on Monin–Obukhov similarity theory and Townsend’s attached eddy hypothesis. *Journal of the Atmospheric Sciences*, *75*(10), 3403–3431. <https://doi.org/10.1175/JAS-D-17-0301.1>
- Lin, C.-L., McWilliams, J. C., Moeng, C.-H., & Sullivan, P. P. (1996). Coherent structures and dynamics in a neutrally stratified planetary boundary layer flow. *Physics of Fluids*, *8*(10), 2626–2639. <https://doi.org/10.1063/1.869048>
- Lindzen, R. S., & Nigam, S. (1987). On the role of sea surface temperature gradients in forcing low-level winds and convergence in the tropics. *American Meteorological Society*, *44*(17), 2418–2436. [https://doi.org/10.1175/1520-0469\(1987\)044%3C2418:OTROSS%3E2.0.CO;2](https://doi.org/10.1175/1520-0469(1987)044%3C2418:OTROSS%3E2.0.CO;2)
- Masson, V., Le Moigne, P., Martin, E., Faroux, S., Alias, A., Alkama, R., et al. (2013). The SURFEXv7.2 land and ocean surface platform for coupled or offline simulation of earth surface variables and fluxes. *Geoscientific Model Development*, *6*(4), 929–960. <https://doi.org/10.5194/gmd-6-929-2013>
- Nuijens, L., Wenegrat, J. O., Lopez Dekker, P., Pasquero, C., O’Neill, L. W., Arduin, F., et al. (2024). *The air-sea interaction (ASI) sub-mesoscale: Physics and impact* (Technical Report). NSF National Center for Atmospheric Research. <https://doi.org/10.5065/78AC-QD31>
- O’Neill, L. W., Chelton, D. B., & Esbensen, S. K. (2012). Covariability of surface wind and stress responses to sea surface temperature fronts. *Journal of Climate*, *25*(17), 5916–5942. <https://doi.org/10.1175/JCLI-D-11-00230.1>
- Perlin, N., Kamenkovich, I., Gao, Y., & Kirtman, B. P. (2020). A study of mesoscale air–sea interaction in the Southern Ocean with a regional coupled model. *Ocean Modelling*, *153*, 101660. <https://doi.org/10.1016/j.oceamod.2020.101660>
- Pinty, J.-P., & Jabouille, P. (1998). A mixed-phase cloud parameterization for use in a mesoscale non-hydrostatic model: Simulations of a squall line and of orographic precipitation. *American Meteorological Society*, 217–220.
- Plagge, A., Edson, J. B., & Vandemark, D. (2016). In situ and satellite evaluation of air–sea flux variation near ocean temperature gradients. *Journal of Climate*, *29*(4), 1583–1602. <https://doi.org/10.1175/JCLI-D-15-0489.1>
- Redelsperger, J.-L., Bouin, M.-N., Pianezze, J., Garnier, V., & Marié, L. (2019). Impact of a sharp, small-scale SST front on the marine atmospheric boundary layer on the Iroise Sea: Analysis from a hectometric simulation. *Quarterly Journal of the Royal Meteorological Society*, *145*(725), 3692–3714. <https://doi.org/10.1002/qj.3650>
- Salesky, S. T., Chamecki, M., & Bou-Zeid, E. (2017). On the nature of the transition between roll and cellular organization in the convective boundary layer. *Boundary-Layer Meteorology*, *163*(1), 41–68. <https://doi.org/10.1007/s10546-016-0220-3>
- Samelson, R. M., Skillingstad, E. D., Chelton, D. B., Esbensen, S. K., O’Neill, L. W., & Thum, N. (2006). On the coupling of wind stress and sea surface temperature. *Journal of Climate*, *19*(8), 1557–1566. <https://doi.org/10.1175/JCLI3682.1>
- Schmidt, H., & Schumann, U. (1989). Coherent structure of the convective boundary layer derived from large-eddy simulations. *Journal of Fluid Mechanics*, *200*, 511–562. <https://doi.org/10.1017/S0022112089000753>
- Singh Khalsa, S. J., & Greenhut, G. K. (1989). Atmospheric turbulence structure in the vicinity of an oceanic front. *Journal of Geophysical Research*, *94*(C4), 4913–4922. <https://doi.org/10.1029/JC094iC04p04913>
- Skyllingstad, E. D., Vickers, D., Mahrt, L., & Samelson, R. (2007). Effects of mesoscale sea-surface temperature fronts on the marine atmospheric boundary layer. *Boundary-Layer Meteorology*, *123*(2), 219–237. <https://doi.org/10.1007/s10546-006-9127-8>
- Stull, R. B. (1988). *An introduction to boundary layer meteorology*. Dordrecht: Springer.
- Sullivan, P. P., McWilliams, J. C., Weil, J. C., Patton, E. G., & Fernando, H. J. S. (2020). Marine boundary layers above heterogeneous SST: Across-front winds. *Journal of the Atmospheric Sciences*, *77*(12), 4251–4275. <https://doi.org/10.1175/JAS-D-20-0062.1>
- Sullivan, P. P., McWilliams, J. C., Weil, J. C., Patton, E. G., & Fernando, H. J. S. (2021). Marine boundary layers above heterogeneous SST: Alongfront Winds. *Journal of the Atmospheric Sciences*, *78*(10), 3297–3315. <https://doi.org/10.1175/JAS-D-21-0072.1>
- Sullivan, P. P., Moeng, C.-H., Stevens, B., Lenschow, D. H., & Mayor, S. D. (1998). Structure of the entrainment zone capping the convective atmospheric boundary layer. *Journal of the Atmospheric Sciences*, *55*(19), 3042–3064. [https://doi.org/10.1175/1520-0469\(1998\)055\(3042:SOTEZC\)2.0.CO;2](https://doi.org/10.1175/1520-0469(1998)055(3042:SOTEZC)2.0.CO;2)
- Villas Bôas, A. B., Arduin, F., Ayet, A., Bourassa, M. A., Brandt, P., Chapron, B., et al. (2019). Integrated observations of global surface winds, currents, and waves: Requirements and challenges for the next decade. *Frontiers in Marine Science*, *6*, 425. <https://doi.org/10.3389/fmars.2019.00425>
- Wallace, J. M., Mitchell, T. P., & Deser, C. (1989). The influence of sea-surface temperature on surface wind in the eastern equatorial pacific: Seasonal and interannual variability. *Journal of Climate*, *2*(12), 1492–1499. [https://doi.org/10.1175/1520-0442\(1989\)002\(1492:TIOSS\)2.0.CO;2](https://doi.org/10.1175/1520-0442(1989)002(1492:TIOSS)2.0.CO;2)
- Wang, S., & Stevens, B. (2000). Top-hat representation of turbulence statistics in cloud-topped boundary layers: A large eddy simulation study. *Journal of the Atmospheric Sciences*, *57*(3), 423–441. [https://doi.org/10.1175/1520-0469\(2000\)057\(0423:THROTS\)2.0.CO;2](https://doi.org/10.1175/1520-0469(2000)057(0423:THROTS)2.0.CO;2)
- Watanabe, S.-I. I., Niino, H., & Spengler, T. (2022). Formation of maritime convergence zones within cold air outbreaks due to the shape of the coastline or sea ice edge. *Quarterly Journal of the Royal Meteorological Society*, *148*(746), 2546–2562. <https://doi.org/10.1002/qj.4324>
- Weinkaemmerer, J., Göbel, M., Serafin, S., Đurán, I. B., & Schmidli, J. (2023). Boundary-layer plumes over mountainous terrain in idealized Large-Eddy Simulations. *Quarterly Journal of the Royal Meteorological Society*, *149*(757), 3183–3197. <https://doi.org/10.1002/qj.4551>
- Wenegrat, J. O., & Arthur, R. S. (2018). Response of the atmospheric boundary layer to submesoscale sea surface temperature fronts. *Geophysical Research Letters*, *45*(24), 13505–13512. <https://doi.org/10.1029/2018GL081034>
- Wenta, M., & Herman, A. (2018). The influence of the spatial distribution of leads and ice floes on the atmospheric boundary layer over fragmented sea ice. *Annals of Glaciology*, *59*(76pt2), 213–230. <https://doi.org/10.1017/aog.2018.15>
- Wyngaard, J. (2010). *Turbulence in the atmosphere*. Cambridge University Press.
- Yang, H., Chen, Z., Sun, S., Li, M., Cai, W., Wu, L., et al. (2024). Observations reveal intense air-sea exchanges over submesoscale ocean front. *Geophysical Research Letters*, *51*(2), e2023GL106840. <https://doi.org/10.1029/2023GL106840>